The design of high-speed and multi-scale *in vivo* retinal imaging with wavefront sensorless adaptive optics optical coherence tomography

by

JiHoon Kwon

B.A.Sc., University of Seoul, 2015

Thesis Submitted in Partial Fulfillment of the
Requirements for the Degree of
Master of Applied Science

in the
School of Engineering Science
Faculty of Applied Sciences

SIMON FRASER UNIVERSITY
Spring 2023

Declaration of Committee

Name:	**JiHoon Kwon**
Degree:	**Master of Applied Science**
Title:	**The design of high-speed and multi-scale *in vivo* retinal imaging with wavefront sensorless adaptive optics optical coherence tomography**
Committee:	**Chair: Yifan Jian** Assistant Professor, Biomedical Engineering Oregon Health & Science University
	Marinko V. Sarunic Supervisor Professor, Engineering Science
	MyeongJin Ju Committee Member Professor, Biomedical Engineering University of British Columbia
	Pierre Lane Examiner Associate Professor, Engineering Science

Ethics Statement

The author, whose name appears on the title page of this work, has obtained, for the research described in this work, either:

a. human research ethics approval from the Simon Fraser University Office of Research Ethics

or

b. advance approval of the animal care protocol from the University Animal Care Committee of Simon Fraser University

or has conducted the research

c. as a co-investigator, collaborator, or research assistant in a research project approved in advance.

A copy of the approval letter has been filed with the Theses Office of the University Library at the time of submission of this thesis or project.

The original application for approval and letter of approval are filed with the relevant offices. Inquiries may be directed to those authorities.

Simon Fraser University Library
Burnaby, British Columbia, Canada

Update Spring 2016

Abstract

Human retinal imaging is rapidly growing industry due to the special characteristics of the eye which has irreversible vision-robbing diseases. Optical Coherence Tomography (OCT) is routinely applied for retinal imaging since it provides three-dimensional retinal images non-invasively. With advancements of the technology, current commercial OCT systems in clinics are able to zoom in and out the region of interest, visualizing and acquiring various features of the retina image in several seconds. However, still there are limitations of achievable imaging angle, image quality and acquisition speed that need to be improved. In this thesis, we introduce the multi-scale feature, adjusting the beam diameter (and hence the resolution) to match each field-of-view to improve the image quality. Furthermore, this system employed a recently developed light source which provides much faster imaging speed which is critical to minimize motion artifacts, providing various potential to enhance the image quality.

Keywords: Laser; Optical coherence tomography; Retinal imaging; Mode-locked laser; Eye investigation; In vivo imaging

Acknowledgments

This thesis has been supported by various members of our lab, Biomedical Optics Research Group (BORG), some of whom I would like to sincerely thank.

First of foremost, I would like to express my gratitude to my supervisor, Dr Marinko V. Sarunic, for allowing me to conduct simulations and all on the lab experiments even upon this COVID-19 pandemic. He has guided and supported me throughout the progress of my thesis with his profession and patience. Also, I would like to thank to Dr. MyeongJin Ju who guided and gave me hands-on experiences to be familiar with optical components for safety and exclusive skills that he has.

I am very proud of myself being a member of BORG and I am specifically grateful to my colleague of BORG, Ms. Destiny Hsu who also contributed her efforts for my research and guided to enhance my English as it is my second language.

Lastly, I would like to thank to all members of BORG for supporting me throughout my degree in this lab.

Table of Contents

List of Tables

List of Figures

List of Symbols

l_c	Axial Resolution
λ_0	Central Wavelength
$\Delta\lambda$	Bandwidth of the Source
z_{max}	Imaging Depth
N_s	Numbers of Sampling Points in Depth
$\delta\lambda$	Sampling Intervals of Spectrum
Δx	Lateral Resolution
b	Depth of Focus
w_0	Waist of Beam
ρ_i	Reflectivity of the sample
ρ_R	Reflectivity of the reference
δ	Dirac delta function
z_0	Common reflection point
z_R	Optical distance from the common reflection point
$\widehat{E_D}$	Fourier transformed photocurrent function
v	Optical frequency
$\mathcal{F}$	Fourier transform
K	Absolute value of the scattering wave vector
k	Scattering wave vector
τ	Acquisition time
c. c.	Complex conjugate artifact
I_D	Intensity profiles of the detector

List of Acronyms

AMD	Age-related Macular Degeneration
DR	Diabetic Retinopathy
RP	Retinitis Pigmentosa
OCT	Optical Coherence Tomography
3D	3-Dimensional
OCTA	Optical Coherence Tomography Angiography
PS-OCT	Polarization-Sensitive Optical Coherence Tomography
RPE	Retinal Pigment Epithelium
NFL	Nerve Fibre Layer
FOV	Field of View
AO	Adaptive Optics
SHWFS	Shack-Hartmann Wavefront Sensor
DM	Deformable Mirror
SAO	Sensorless Adaptive Optics
FDML	Fourier Domain Mode-locked Laser
OPD	Optical Pathlength Difference
TD-OCT	Time Domain Optical Coherence Tomography
FD-OCT	Fourier Domain Optical Coherence Tomography
SD	Spectral Domain
SS	Swept Source
VIS-OCT	Visible Light Optical Coherence Tomography
NIR	Near Infra Red
SNR	Signal-to-Noise Ratio
NA	Numerical Aperture
MAL	Multi-actuator Adaptive Lens
VFL	Variable Focus Lens
PDDU	Polarization Diversity Detection Unit
DOPU	Degree Of Polarization Uniformity
GVD	Group Velocity Dispersion
ANSI	American National Standards Institute
VISTA	Variable Inter Scan Time Analysis
BM-scan	Multiple B-scans

Chapter 1. Introduction

1.1. Anatomy of the eye

Vision is our most valuable sense, and the eye enables visual sensing. Figure 1-1 shows the anatomy of the human eye. The cornea and pupil focus light onto the retina that transforms the images into electric signals, and then transmits them to the brain. The cornea, which has a dome-shape, works as a structural barrier and delivers light into the retina via refraction. Once light passes the cornea, the pupil is controlled by the iris which adjusts its size to accept a suitable amount of light. The general size of the pupil is from 1 to 4 mm in daylight conditions. The intraocular (crystalline) lens behind the pupil adds additional focus for the light into the retina which is located in the back of the eye. The vitreous region between the retina and pupil is around 20 mm thick.

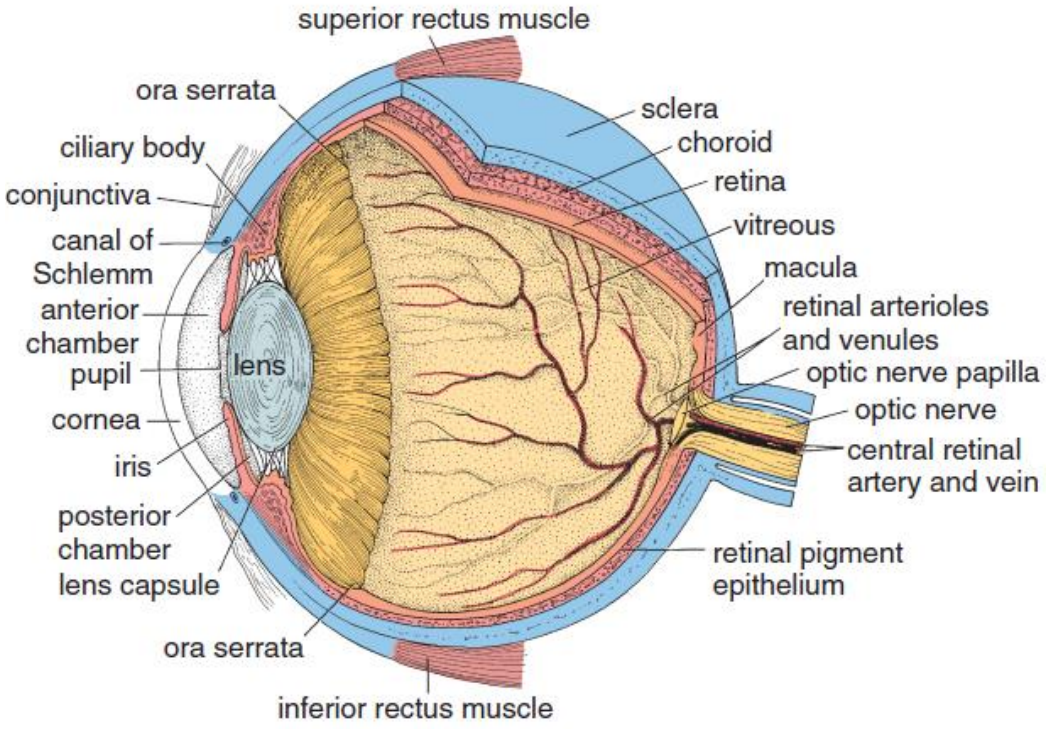

Figure 1-1 Anatomy of the human eye [1].

Figure 1-2 shows a representative histological cross-section of the retina [2]. The retina serves as the detector of the eye and has various cell layers and vessel networks. For instance, the capillary beds located above the outer nuclear layer (ONL) provide nutrients and collect waste from nearby tissues. The retinal pigment epithelium (RPE) which is located beneath the photoreceptors, divides the choroidal and retinal layers and transports important nutrients into the retina from the choroid. Surprisingly, all of these tissues exist within a small thickness of approximately 250 micrometers [3]. In addition, various vision-lowering diseases (glaucoma, age-related macular degeneration (AMD), and diabetic retinopathy (DR)) occur in the retina. To accurately diagnose such diseases, there is a need to develop precise retinal imaging technology.

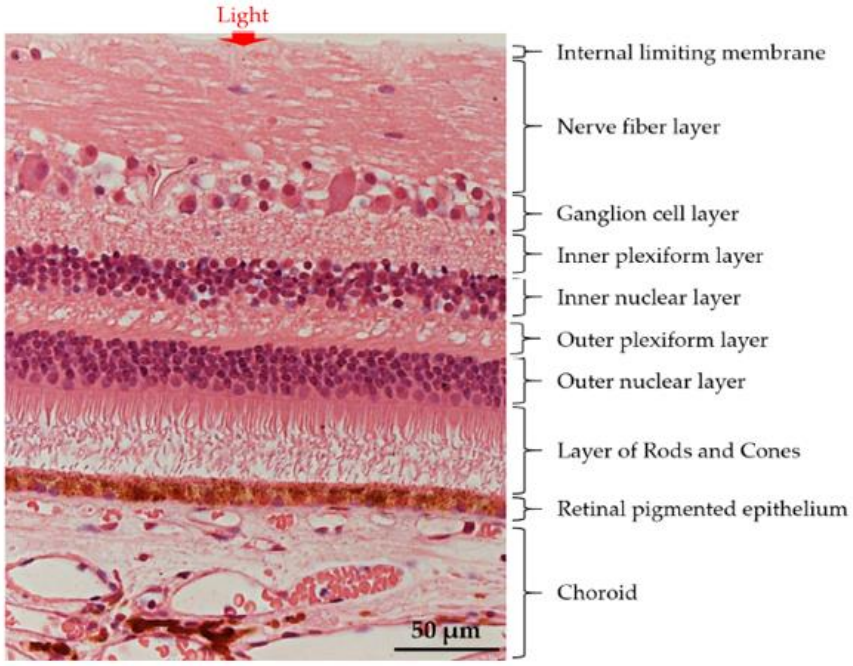

Figure 1-2 The cross-sectional image of the retina [4].

1.2. Development of retinal imaging modalities

Two of the most common retinal imaging devices are fundus photography (FP), and fluorescein angiography (FA). FP acquires 2-dimensional images of the retina, and it is used as a standard imaging tool in the clinic due to its ease and low-cost imaging capability [5], [6]. FA applies a special dye to specifically visualize the vasculature. Many research groups successfully showed the performance of FA, assisting eye doctors with

more valuable information [7]–[9]. Figure 1-2 shows representative images of both FA and FP [10].

Figure 1-3 3-D volumetric data acquisition with OCT [10].

However, more recently developed optical coherence tomography (OCT) provides reconstructed three-dimensional images by calculating interfered signals of light, unlike FA or FP. Technically, OCT shines lights into the patient eye and collects the back-reflected signal from the sample. This sample signal then is interfered with a reference signal, generating interferometric fringes at a photodetector. This signal provides depth information (an A-scan) at a single location. By scanning the position of the focus across the retina, a cross-sectional image (B-scan) can be generated, which is useful to investigate the layers in the retina. Then, a 3-D volumetric image can be acquired as a set of B-scans. Figure 1-4 shows the way of OCT scans from an A-scan to 3-D volumetric data.

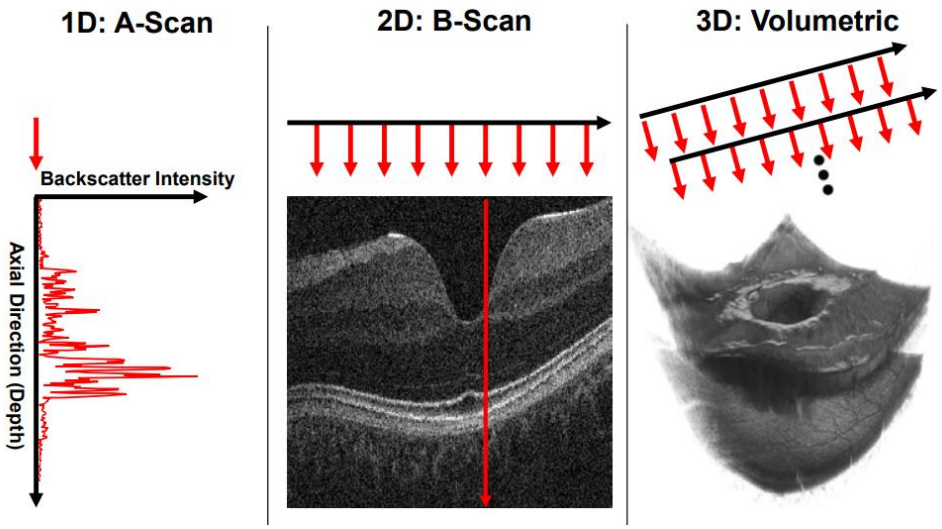

Figure 1-4 3-D volumetric data acquisition with OCT; depth direction intensity profile (A-scan, left), cross-sectional 2-D image that comprises sets of A-scans (B-scan, center), and 3-D volumetric data by scanning lateral direction (right) [11]**.**

There have been various technical advancements in OCT including functional extensions. Among the developments, OCT Angiography (OCTA) captures B-scan images consecutively at the same location to identify more detailed blood flow information, eliminating the requirement of special dye as in FA. With this method, OCTA can assist eye doctors to investigate retinal diseases. Additionally, adaptive optics (AO) technology assists in further increasing the quality of OCTA images. Historically, AO was first used in astronomy to remove the atmospheric turbulence on images in ground-based telescopes [12], [13]. The elimination of the turbulence allowed diffraction-limited imaging from the ground. In OCT, the aberrations caused by the eye are corrected by this technique, resulting in a significant improvement in vascular images.

Another functional extension is polarization-sensitive OCT (PS-OCT) which facilitates exclusively detecting certain layers in the retina. PS-OCT uses polarization characteristics of the light such as phase retardation and depolarization. Several groups successfully revealed RPE and nerve fiber layers (NFL) which conduct their specific roles in the human eye with PS-OCT [14]–[18]. The potential of PS-OCT was brought to the attention of researchers, and various optical components (fibers or polarizers) were employed in the PS-OCT. Especially, polarization diversity detection (PDD) uses simple

bulk or fiber optic components to interpret the depolarization effect [19]–[21]. The first report that PDD is utilized and detected depolarization effect in the retina was identified in the RPE layer [22]. Later, many literature report this phenomenon (depolarization effect) is caused by melanin component in RPE layer which scrambles the polarization state of the light (randomization) [17], [18], [21]–[24]. As mentioned earlier, RPE is directly related to AMD, and the identification of this layer helped the observation of mild drusen which is a biomarker of AMD (dry type).

However, one of the drawbacks of existing OCT systems lie in the fixed beam size. In general, OCT systems cannot modify the size of the incident beam, causing the limitation on obtaining the optimal resolution according to the target to be imaged (resolution is proportional to the size of the beam). For instance, based on the eyes, the size of the object defers from several micrometers (micro vessels / capillaries) to several tens of micrometers (blood vessels). To obtain optimal resolution images of these objects, the size of the incident beam and the field of view must also be adjusted.

Practically, in OCT designs, the depth of focus has a significant impact on the performance of the system. In OCT, the depth of focus is inversely proportional to the size of the incident beam. When employing a large incident beam, depth information is limited. If the depth of focus is too small, it becomes difficult to acquire a larger area on the retina due to limited isoplanatic patch and the curved shape of the eye. For wide field-of-view (FOV) scanning, the curvature the eye is apparent in the B-scan images, and a larger depth of focus (hence a narrower incident beam on the cornea) is required.

1.3. Motivation

The motivation of this thesis is to upgrade our previously reported, a multi-scale and -contrast imaging system [25]. Multi-scale refers the adjustable resolution which is derived by changing the size of input beam diameter at the cornea. The system developed in this research used 'zoomable collimator' which allowed to change the size of incident beam. By doing so, it became possible to achieve each suitable resolution in different FOVs.

As result, for narrower FOVs, deep capillaries were observable with higher incident beam size (better resolution). Furthermore, this system allowed to acquire up to

9 mm² size of the retina while minimizing the penalties of depth of focus. Meanwhile, to further improve the sharpness of the image, transmissive AO tools were investigated, which minimized the effects of aberrations. It successfully enhanced the image quality of deep capillaries (which will be discussed in Chapter 3).

The system in Ref. [25] had several drawbacks. Though the image size in wide FOV (9mm²) is quite large, it is not possible to cover whole area of the retina. Considering recent commercial devices can cover up to 12 ~ 15 mm², still this device needs further improvement to provide wider area imaging mode [26]–[28]. Moreover, this system used a 100kHz wavelength swept laser, and the large FOV acquisition time was ~10 seconds, which is quite longer than that of current clinical instruments.

Therefore, in this thesis we will present a new system design that improves the achievable FOVs, while maintaining a high-resolution image. Based on computer aided simulations, this new system can achieve up to 12.5 mm² (~38 in degrees at the retina). Also, the light source is replaced with a novel FDML laser which is 16x faster than previous sweeping laser. Lastly, for faster optimization, this system employed reflective AO device which has higher strokes and better response time.

1.4. Thesis Organization

The organization of my thesis is as follows. Chapter 2 contains the background and introduction of the important optical properties of OCT when considering a new design as well as application examples. Chapter 3 shows a brief explanation of my preliminary work that was conducted in preparation to this thesis. Chapter 4 explains several simulations and related experiments to achieve the goal of this thesis. Chapter 5 is the discussion section that wraps up the results from Chapter 4 and suggests the ideal imaging protocol with the OCT system.

1.5. My contribution of the thesis

My work on the thesis was the design and alignment of the optical system and data acquisition. I participated in the development of two systems that were designed for human and mouse retina imaging. Both were presented at academic conferences, and published in two journals [25], [29]. After evaluation of these experimental designs, a new system for this thesis was expanded from the human retina imaging project to a more advanced version. The wavefront-correction algorithm used here was not developed by me and I would like to give gratitude to the developers [8], [30]–[32].

Chapter 2. Optical coherence tomography (OCT)

2.1. Theory of OCT

As discussed in the previous Chapter, OCT delivers the light from the source to the pupil of the eye and interprets the back-reflected signals from the tissue using low coherence interferometry. The Michelson interferometer is a basic component of OCT interferometry that was developed by Albert A. Michelson in 1881. Figure 2-1 shows an example of a Michelson interferometer, containing a beam-splitter, two mirrors, and a photodiode detector. The beam-splitter serves to split the beam into the desired proportions (50/50 in general) and delivers the light from the source into two different paths by reflection and transmission. This light is reflected from two mirrors (reference and sample) and gathered into a photodiode detector to be recorded in an interfered signal pattern. To generate the low coherence interfered signal, the reference mirror has an adjustable stage that enables matching the path-length differences between two mirrors ($Z_r = Z_s$). When the optical path length (OPD) is mismatched, there is no interference signal in the analog-to-digital converter (just the DC component), whereas if OPD is matched the interference signal can be interpreted to reconstruct a depth-resolved image. This method of scanning (mechanically moving reference mirror) to reconstruct the images is called time-domain OCT (TD-OCT). However, due to the mechanical requirements to adjust the position of the reference mirror, TD-OCT has a significant drawback of low imaging speed.

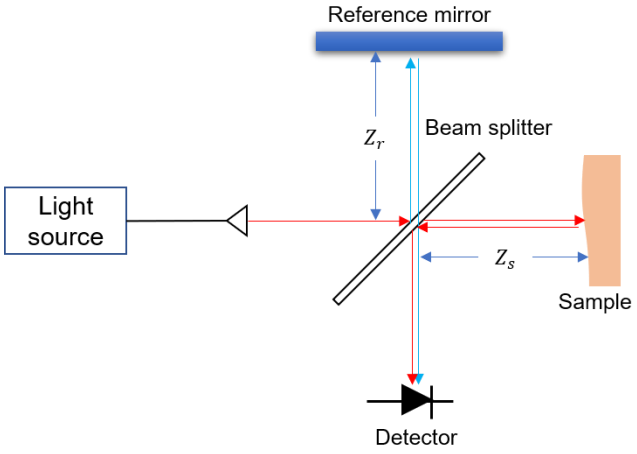

Figure 2-1 Michelson interferometer [33]**.**

Fourier Domain OCT (FD-OCT) is an advanced OCT method that removes the need for adjustment of the reference mirror position. Instead of moving the reference mirror, FD-OCT interprets the signal in the wave number domain by implementing the Fourier Transform. The Fourier transformed signal can contain multiple interfered signals in different location from zero-delay (where the OPD is perfectly matched). Hence, FD-OCT enables higher speed imaging and hence the quality of the image has been dramatically improved [34]. FD-OCT can be implemented in two different ways, which are called Spectral Domain (SD) or Swept Source (SS) [34]. SD-OCT uses an optical grating element which spreads the interfered signal depending on wavelength and a high-speed line scan camera detects these interferograms. On the other hand, SS-OCT, which is also used in this thesis, uses a narrow band filter in the source cavity, and tunes this filter to sweep across the whole spectrum within micro-seconds, enabling high-speed image acquisition. A brief introduction to the swept source will be explained in the following subchapter.

Even though FD-OCT enables high-speed imaging, another important factor to achieve is high-resolution imaging when we design the OCT system. In the OCT, the axial and lateral resolutions are separated from each other, which enables improving image quality in both depth and lateral direction. In depth-direction, axial resolution and penetration depth are mainly affected by the characteristics of the light source. Equation 2-1 shows the relationship between axial resolution (l_c) and the light source, and the l_c is dependent on central wavelength (λ_0) and bandwidth ($\Delta\lambda$), where n is the refractive indices of the sample. Therefore, the bandwidth and central wavelength of the light determines the quality of the image in depth direction.

$$l_c = \frac{2ln2\lambda_0^2}{n\pi\Delta\lambda} \qquad \text{Eq. 2-1}$$

Penetration depth is the term of how deeply the OCT device can visualize in the depth direction, and it is mainly affected by the scattering and absorption characteristics of the retina and eye based on the central wavelength of the light source. Figure 2-2 shows the curve of the absorption coefficient for representative sample tissue components, and the blue curve is the absorption of water [35]. Since the human a retina is covered by water, which is in the vitreous gel, water is the main factor that

absorbs light. Though visible light wavelengths have lower absorption by water, the light intensity at these wavelengths is strictly limited by the amount of permissible optical power due to the possibility of injury. Therefore, longer wavelengths are preferred in retinal imaging (normally 840 or 1060 nm ranges). Additionally, the scattering effect attenuates the light and hinders the penetration depth. Specifically, this affects light penetration capability more dominantly compared with the absorption of water [33], [36]. This tendency is significantly higher in the visible wavelengths relative to the near-infrared (NIR). Consequently, a NIR wavelength light (1060 nm) is chosen as the light source in this thesis.

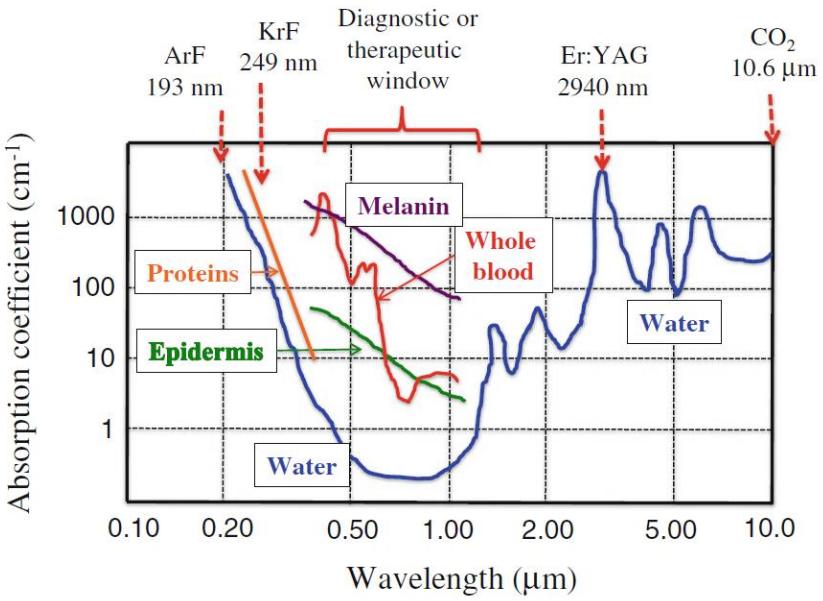

Figure 2-2 Absorption coefficient with different samples [35]**.**

Along with penetration depth, axial imaging depth is another factor that needs to be considered. Equation 2-2 explains the maximum imaging depth (z_{max}) which is related to the properties of the light source and detection [37].

$$z_{max} = \frac{n}{4}\frac{\lambda_0^2}{\Delta\lambda}N_s \qquad \text{where } N_s = \frac{\Delta\lambda}{\delta\lambda} \qquad \text{Eq. 2-2}$$

Here, N_s is the total number of sampling points (sampling density) that divides the spectrum of the light source and $\delta\lambda$ is the interval between samplings of the spectrum. As the Equation 2-2 shows, a narrower $\delta\lambda$ increases the achievable imaging

depth. And securing sufficient imaging depth range permits easy capturing the entire layers of the retina in wide area scanning (the curvature of the eye appears). However, the narrower $\delta\lambda$ induces a higher N_s, and this N_s increases both data size (computation time) and may affect the image acquisition time. This causes more eye motions during image acquisition, which degrades the image quality. On the contrary, to correctly generate the cross-sectional image, there is minimum sampling density based on Nyquist Theorem [33] as well. Hence, it is important to choose optimal sampling density to achieve both imaging depth and fast image acquisition speed.

The lateral resolution is influenced by the numerical aperture (NA), and the NA is defined by the refractive index (n) and the angle of the focused beam ($sin\theta$) that is delivered into the sample as shown in Equation 2-3 and 2-4 [35].

$$(\Delta x) = 0.51\frac{\lambda}{NA} \qquad \text{Eq. 2-3}$$

$$NA = n\,\sin\theta \qquad \text{Eq. 2-4}$$

The $sin\theta$ is the value of half-angle of the incident beam at the sample, as described in Fig. 2-3 [38]. For retinal OCT, since the distance from the crystalline lens to the retina (target sample) is fixed, the lateral resolution is solely influenced by the beam diameters (changes NA) at the cornea. As such, even though higher beam diameters could provide a higher lateral resolution, the aberration of the eye is pronounced as well, hindering the image quality (details in Chapter 2.2.2). Therefore, carefully choosing the proper beam diameter is critical in optical designing.

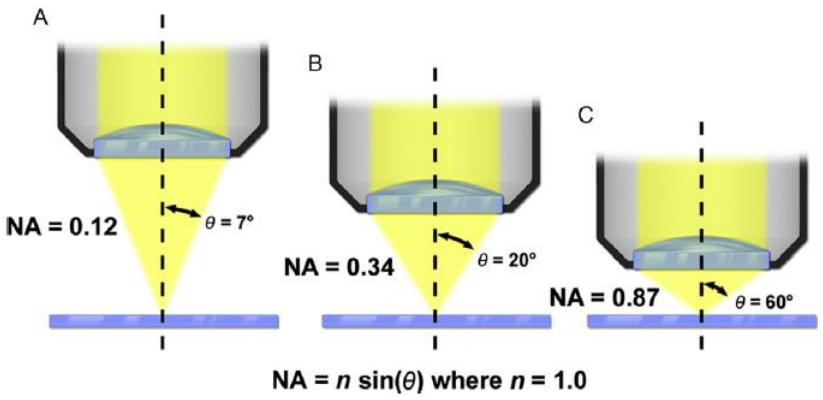

Figure 2-3 Numerical aperture and working distance [38]**.**

In photography, the depth of focus indicates the range of which focal plane can be shifted without degradation in image quality. In OCT, the depth of focus (b) is determined by the Rayleigh length of the beam waist and is inversely proportional to the numerical aperture (NA), as shown in Equation 2-5. The w_0 is a waist of a beam, λ_0 is the central wavelength of the source, n is the refractive index [33]. Since the human retina has curvature, sufficient depth of focus is essential to capture major layers of the retina in wide FOV.

$$b = \frac{2\pi n}{\lambda_0} w_0^2 = \frac{n\lambda_0}{2\pi(NA)^2}. \quad \text{Eq. 2-5}$$

Figure 2-4 illustrates the presence of the curvature of the eye in the cross-sectional image in wide FOV (a) compared with narrow FOV (b). The top row is *en face* view of each cross-sectional (B-scan) image of the bottom row and the wide (a) and narrow (b) FOV are 6 × 6 mm and 3 × 3 mm, respectively. The curvature of the eye expands the start/end points of the layers of the retina in the axial direction, as shown in Fig. 2-4. This phenomenon goes even larger in the wider FOV modes. Practically, when designing the sample arm of OCT, the objective lenses typically influence the beam diameter which decides the value of NA. Therefore, we conducted a simulation with an optical program (ZEMAX) to provide systems that fit the goal of this thesis, and details of this will be discussed in Chapter 4.

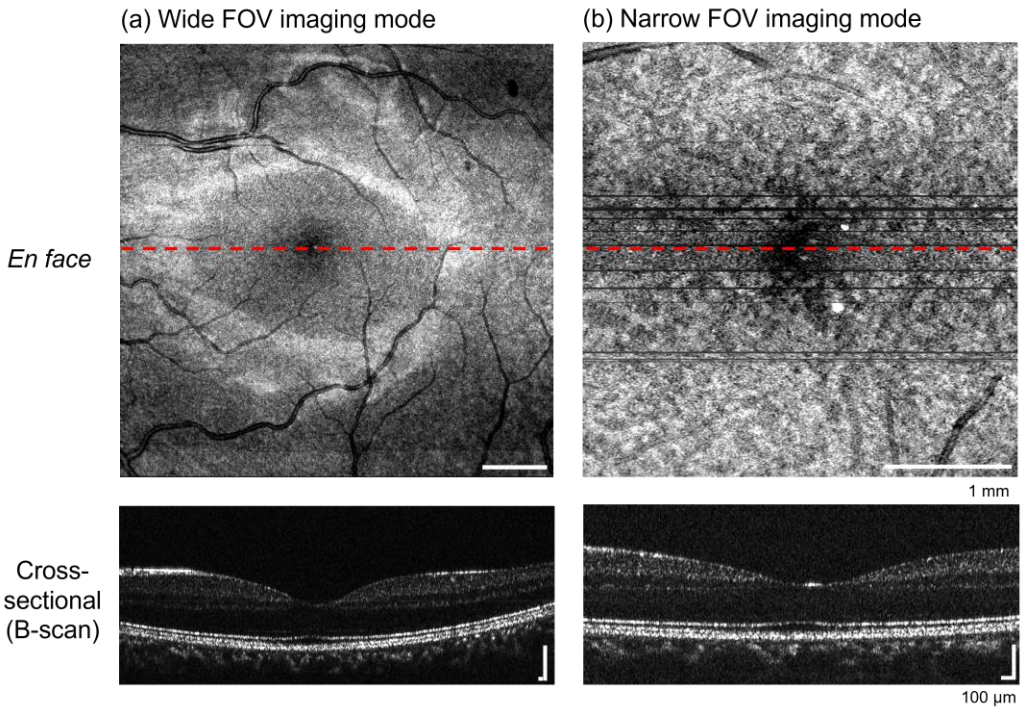

Figure 2-4 Curvature of the retina with wide FOV (a) compared with narrow FOV (b) in cross-sectional (bottom) and its *en face* image (top). Each FOV size is 6 × 6 mm (a) and 3 × 3 mm (b).

2.2. Retinal OCT

As discussed in the previous subchapter, high-speed and high-resolution is the key component in retinal OCT to provide a high-quality image. In this subchapter, a brief introduction to high-speed retinal OCT and a resolution of cellular level in retinal OCT will be discussed. In the last subchapter, two representative functional extensions of retinal OCT will be explored.

2.2.1. High-speed Retinal OCT

Increasing the imaging speed of retinal OCT is one of the key factors to acquire a high-quality image since it diminishes the motion of the eye. Nowadays, SS-OCT achieved up to several mega-hertz scanning speeds by developing various methods to upgrade the speed of tuning filters in the laser source. The first generation of SS-OCT utilized rotating polygon mirrors which achieved a 50 kHz A-scan rate. Recently, micro-electromechanical systems (MEMS) based scanning mirrors for wavelength sweep allowed high-speed A-scan rate (100 ~ 200 kHz). Then, the vertical-cavity surface-emitting laser (VCSEL) realized several hundreds of kHz in the 1060 nm wavelength [39].

More recently, a novel Fourier domain mode locking (FDML) enables increasing the sweeping rate up to several megahertz [40]. A representative schematic of the FDML is shown in Fig. 2-5. FDML applies the delaying fiber in the laser cavity to optically store the original frequency sweep, during which the wavelength filter is synchronously tuned to the round-trip time of the cavity. Additionally, a few research groups applied the buffering technique (duplicating the original sweeping pulse) to further increase the sweep rate at ~1.6 MHz [40], [41]. As shown in Fig. 2-6, a series of optical fibers was added after the cavity, generating three replicated wavelength-sweeping pulses. The first buffering stage copies the original sweeping pulse, and the following stage duplicates these two input sweeps (original and copy of first buffer), generating another two sets of buffers.

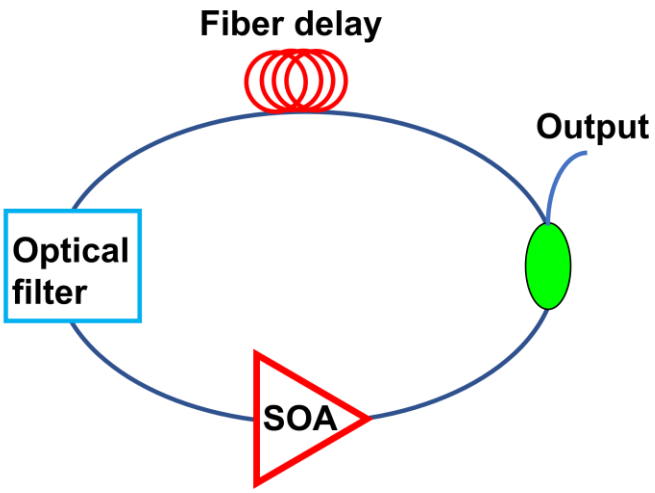

Figure 2-5 Representative schematic of the FDML. SOA (semiconductor optical amplifier) is gain medium and optical filter is wavelength tunable filter.

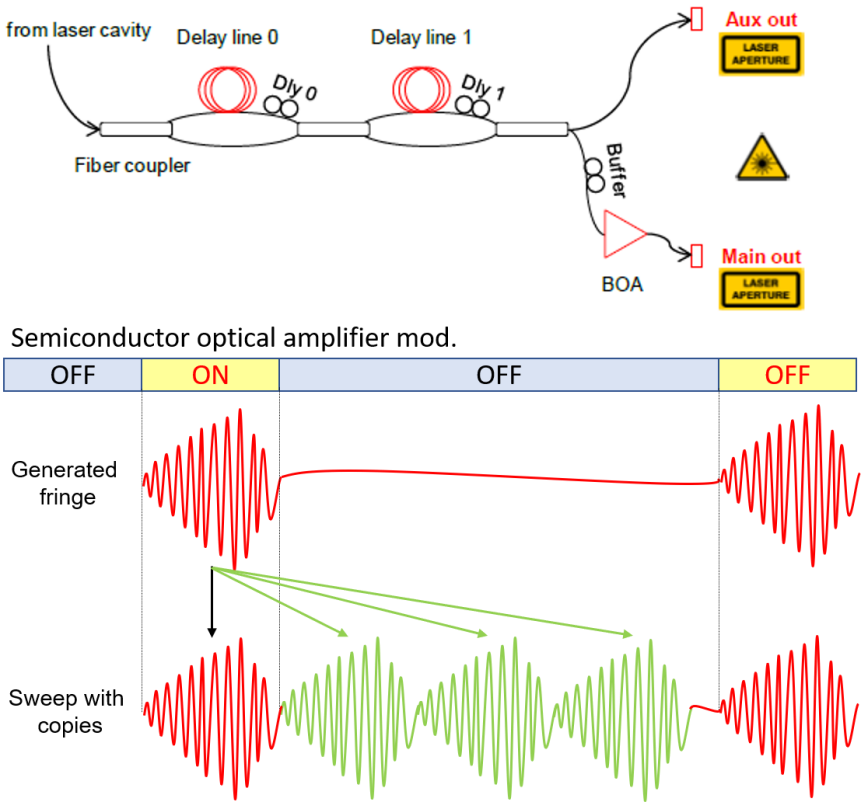

Figure 2-6 FDML laser buffer stage and delay for duplication [42]**.**

Though the higher sweeping speed of this laser has a sensitivity penalty of around 10 to 15 dB from the conventional (lower A-scan rate) SS-OCT system, several

research groups successfully acquired images (enhanced dynamic range) with this laser source [27], [43]. These reports assumed that the reason for the enhancement in OCTA was from fewer motion artifacts due to the higher imaging speed. Also, since the faster swept laser provides relatively motion-free data, it could enable an effective synchronizing process (volume registration), for multi-volume averaging techniques that have been explored by our group [44]. This averaging technique provides higher SNR to overcome the sensitivity penalty caused by a faster A-scan rate, and the SNR improvement is proportional to the square root of the number of averaged frames [45]. Another important property of the FDML that need to be investigated is phase stability. During the buffering stage, there is a possible mismatch between each buffer spectrum. This mismatch induces phase differences in each buffer that could hinder the OCTA quality. Therefore, to tackle this issue, we investigated the effect of the phase stability issue, and the details will be discussed in Chapter 4.3.

2.2.2. Cellular-resolution Retinal OCT

High-resolution of Retinal OCT is important to provide detailed structural and vascular information. However, since it is unavoidable to pass through the crystalline lens of the human eye, aberration always occurs if a higher beam diameter is employed in OCT systems. Aberration is the phenomenon of imperfections on the wavefront of a propagating beam. This induces the blurring or distortion of the image and there are two types of aberration depending on its character, chromatic and monochromatic aberrations. For chromatic aberration, it occurs due to the variation in refractive indexes that the cornea and crystalline lens inherently causes depending on different wavelengths, affecting the focal shift. This type of aberration can be corrected by adopting a lens that has an achromatic character (an achromatizing lens). In the OCT system development, achromatic aberrations are minimized by the use of achromatic lenses, or mirrors, which are not wavelength dependent. On the other hand, monochromatic aberrations are also known as geometric aberrations and are caused by the shape of the lens or mirrors. Human eyes are not perfectly shaped and do not follow the ideal paraxial lens approximation. Therefore, the terms above the second order of the sine function can be modeled to identify the imperfect shape of the wavefront. When it takes into retinal imaging, low-order aberration comes from defocus, astigmatism, and coma, and this adversely influences the image quality[13], [46]. The higher-order

aberrations are related to higher NA (larger beam size). It is because higher NA aids to capture details of the retina within micrometer scales. Hence, these types of aberrations need to be corrected by using adaptive optics. To resolve these issues, adaptive optics (AO) can be employed in retinal OCT.

Adaptive optics (AO) was first developed in astronomy in the 1950s to correct the distortion of light from astronomical sources. The turbulent atmosphere of the Earth hindered the ability of the ground-based telescopes [13] and AO was used to cancel the distorting effect upon the optical wavefront caused by this turbulence. After the successful development of astronomy, adaptive optics was also used in ophthalmic imaging to correct the aberration caused by imperfections in the human eye. As computational technology advanced, AO tools have been used in real-time aberration correction in wavefront by applying devices such as Shack-Hartmann wavefront sensors (SHWS) and deformable mirrors (DM).

Figure 2-7 (a) shows the representative wavefront and Fig. 2-7 (b) illustrates several wavefront distortions that occurred by inherent ocular aberration (hyperopia, myopia, higher-order aberration) compared to the normal case (emmetropia) [47]. In Fig. 2-7 (c), the Zernike polynomials are describing various types of aberration over the unit circle which is convenient to understand the wavefront aberration character. To achieve a diffraction-limited focus, all propagating rays need to converge at the desired focal point. Adaptive optics devices in ocular imaging induce the counter-aberration to correct the inherent aberrations occurred by sample tissue. This gives increased spatial resolution and recovers the distorted image thereby researchers or ophthalmologists can observe better details and features in the image.

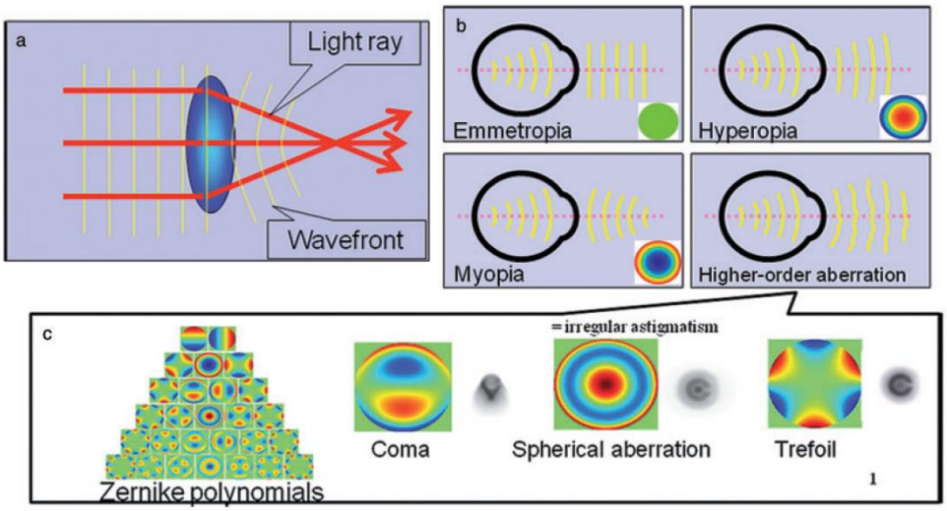

Figure 2-7 Wavefront distortion and related aberrometry [47]**.**

There are various aberration correcting devices in AO, and generally, it can be classified into two different types, transmissive and reflective. These devices again can be described as two different groups for lower/higher order aberration correction. The simplest device, a variable focus lens (VFL) is relatively small and cost-effective, but its weakness is it only correct one type of aberration (defocus). The higher order aberration corrections are required for human retinal imaging with a higher NA, and deformable mirrors (DM) are often used in this case [33]. The DM which is utilized in this thesis provides fast speed and large stroke to correct the aberrations.

To correct the aberration and increase the image quality with AO devices, there are several ways to achieve optimization. In common implementations, adaptive optics in OCT uses the Shack-Hartmann wavefront sensor (SHWS) to directly measure the aberration of the wavefront that is caused by the sample tissue. And this aberration wavefront shape is applied into the deformable mirror (DM) such that it compensates the wavefront distortion. This wavefront correction method can be performed in real-time and is sensitive to wavefront distortion when the aberrations temporally vary. However, since wavefront measurement requires an additional wavefront sensing scheme, it is sensitive to back-reflection of the lenses and to miss-alignment. To avoid this issue, wavefront sensorless adaptive optics (SAO) uses an indirect method via observing the image quality with several metrics such as sharpness and brightness. Several research reports have also used this method [8], [13], [31], [32], [48], [49] since it is cost-effective, and simpler in system design.

2.2.3. Functional Retinal OCT

Functional extensions of OCT provide various benefits in clinic by applying different methods to visualize retinal structures or vasculatures. Among them, OCTA is a non-invasive motion contrast detection method, which uses temporal computation of the differences of the signal detection at a fixed point, visualizing volumetric blood flow information. Since OCTA computes temporal variations, commonly at least two data sets are required to obtain this information. This way of scanning protocol is called as BM-scans (multiple B-scans), and generally, 2 M modes are employed to visualize the vascular information. Occasionally, 4 BM mode is employed to visualize choriocapillaris [41], [43]. Figure 2-8 shows the representative OCTA images of superficial and deep capillary beds from Ref. [50] in which 2 BM scan mode was applied.

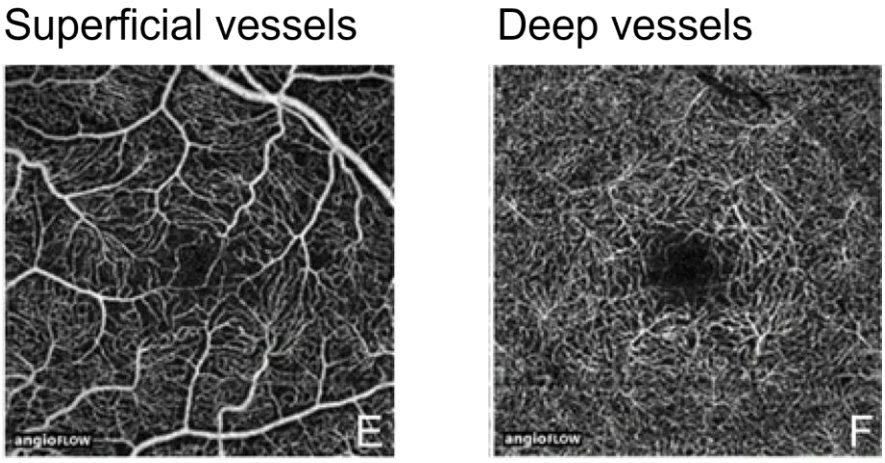

Figure 2-8 OCTA of superficial (left) and deep capillary beds (right). The size of the image is 3 × 3 mm [50]**.**

Though OCTA technology has evolved over the past few years, information that OCTA cannot provide information on the relative blood flow velocity. It is because the time intervals of B-scans are fixed, and this interval delay cannot be changed during the image acquisition. Moreover, allowing more temporal intervals in B-scans requires a longer acquisition time which induces motion artifacts. This kind of limitation in OCTA technique could possibly be resolved by using ultrahigh-speed lasers (FDML for instance).

The FDML laser reduces total scanning duration, which allows more flexibility for the given time intervals (between BM-scans) by each OCT systems. This flexibility is useful for analyzing the correlation between time intervals (in BM-scans) and blood flow. For instance, different time intervals can be applied in each data sets to visualize the differences of the quality of the OCTA. By doing so, we can understand what the ideal time intervals in each B-scans at certain vessel networks in the retina is. A detailed experimental result of this concept will be discussed in Chapter 4.3.

Another functional extension that provides useful contrast information is Polarization-diversity OCT (PD-OCT). PD-OCT is the branch of polarization-sensitive OCT (PS-OCT) that is utilized to exclusively enhance the contrast of certain target layers (NFL and RPE) by acquiring polarization characteristics (birefringence and depolarization). Specifically, PD-OCT visualizes the polarization scrambling effect (depolarization) that randomizes the polarization state of the incident light, and this phenomenon was described in the RPE layer by Pircher *et al.* [51]. Baumann *et al*. investigated a phantom melanin suspension and suggested that the melanin content in RPE is the source of the depolarization effect [23]. To visualize this depolarization effect, PD-OCT utilizes a spatial averaging calculation method which is called a degree of polarization uniformity (DOPU).

DOPU can be analyzed by computing spatial variances of Stokes vectors among neighboring speckles. DOPU value can be quantified by the Stokes vector as it is shown in Equation 2-6 [33] where I, Q, U, V denote the four Stokes vector elements, A_H and A_V are two orthogonally polarized (horizontal and vertical) interference terms at the detectors, and $\Delta\varphi$ is the phase difference in two channels (H / V).

$$S = \begin{pmatrix} I \\ Q \\ U \\ V \end{pmatrix} = \begin{pmatrix} |A_H^2| + |A_V^2| \\ |A_H^2| - |A_V^2| \\ 2A_H A_V cos\Delta\varphi \\ 2A_H A_V sin\Delta\varphi \end{pmatrix} \quad \text{Eq. 2-6}$$

For the complex signal OCT, the U, V terms would be denoted as the real and imaginary parts of multiplication between A_H and A_V^* and $*$ indicates the complex conjugate. Equation 2-7 shows the DOPU measurement via spatially averaging the stokes vector elements over surrounding pixels within a rectangular kernel [33] where indices m represent mean Stokes vector elements.

$$DOPU = \sqrt{(Q_m^2 + U_m^2 + V_m^2)}$$ Eq. 2-7

These spatially averaged DOPU values can vary between 0 to 1. When there is no randomness of polarization (RP) present, the DOPU value becomes 1, representing the interfered signal polarization is preserved. On the contrary, in the presence of depolarization, DOPU goes below 1, indicating the interfered signal is randomly depolarized. The DOPU values identified by these methods can be used to generate the DOPU contrast map. Figure 2-9 shows a representative cross-sectional image that is captured and generated by PD-OCT (acquired from volunteers). Usually, DOPU is colour-coded from red to green (or blue) based on its value. Red (high) indicates no depolarization has been detected in that region, whereas yellow or green (low) explains there is a depolarization effect. On the left of Fig. 2-9, the morphological change of the RPE layer can be easily identified. Since PD-OCT captures morphological changes in the RPE layer effectively, several research reports visualized the RPE layer by using PD-OCT [21], [25], [52]. Our group also used PD-OCT with multi-scale imaging technique, and details of system configuration and post-processing will be discussed in Chapter 3.2.

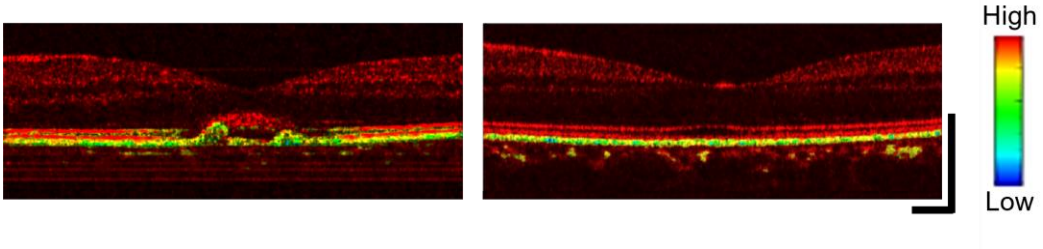

Figure 2-9 Cross-sectional image of overlaid DOPU contrast over intensity-based OCT B-scan from pathological case (left) and healthy case (right). The scale bar is 250 μm [50]**.**

2.2.4. Chapter Summary

This chapter described the fundamental backgrounds of OCT and introduced functional extensions of OCT for visualizing various tissue layers in the retina (especially blood vessels and RPE). In the next chapter, our previously studied multi-scale and -contrast OCT imaging system will be discussed.

Chapter 3. Multi-scale and contrast Retinal OCT

This chapter presents results from a pilot study that motivated the technical design aspects of this thesis. The goal of the pilot study was to utilize an existing multi-scale imaging module that incorporated AO. Additionally, OCTA and PD-OCT contrast was employed to give more valuable information within a single *en face* image [25]. My main contribution to this study was performing simulations with various lens configurations to realize the final design of the imaging system. Then, I assembled and aligned the system to achieve its optimal performance and acquired data for further analysis. The results of this pilot study will be used to determine the design objectives in the next chapter.

3.1. System Overview

Figure 3-1 shows the schematic of the system that was used in the study. The system used a 1060 nm wavelength swept laser source with a 100kHz rate and the beam diameter at the pupil was adjustable ranging from 1 to 3 mm. The adjustable beam diameter was achieved by employing a 'zoomable collimator' (ZC618APC-B, Thorlabs Inc.), which changes the diameter of the collimated beam. Though the zoom collimator was continuously tunable throughout its range, this research used three scaling modes (low, medium, and high NA). The phase-calibration unit served as a interferometer sub-system, which visualized the fringe signal at close to zero delay to correct phase errors caused by the swept laser. Details of the calibration method can be found in the Appendix of Ref. [53].

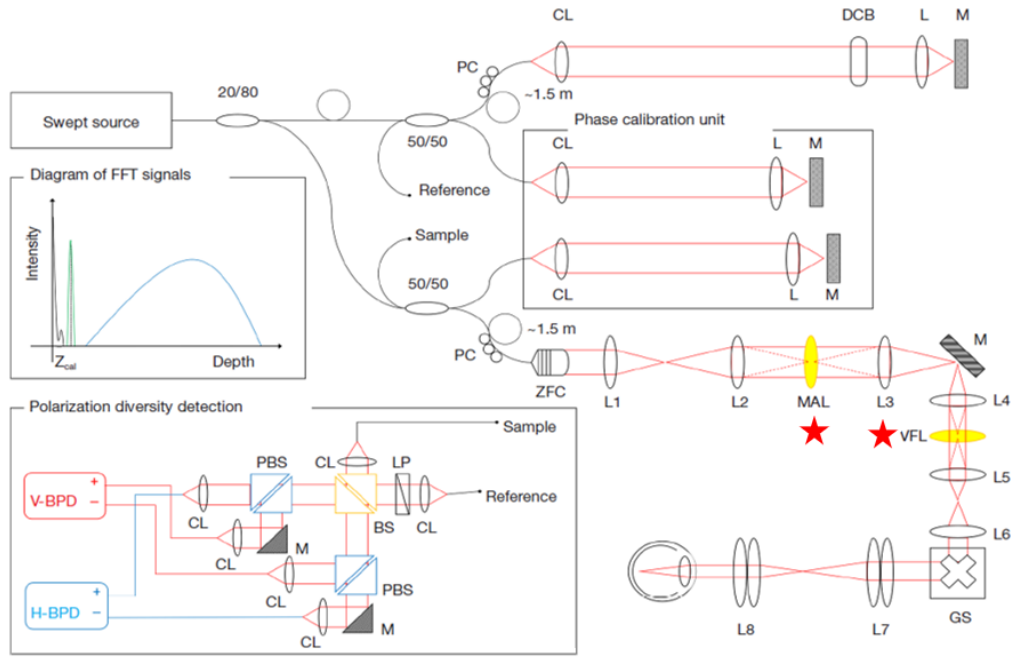

<Sample arm top-view> <Polarization diversity detection unit>

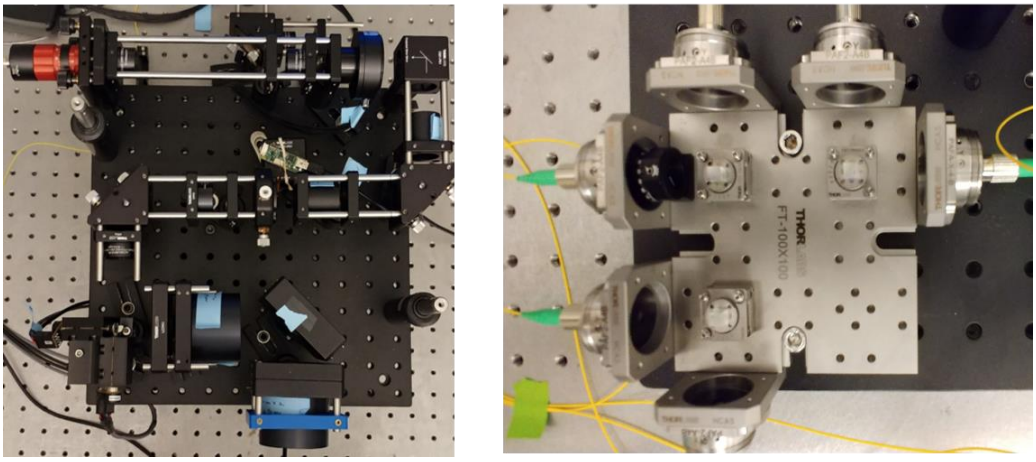

Figure 3-1 Schematic and topology of multi-scale and contrast imaging system.

There are two major components in this system, the AO device to enhance the image quality, and a polarization diversity detection unit (PDD). For AO optimization, two transmissive type lenses were employed in the interferometer, a multi-actuator adaptive lens (MAL) and a variable focus lens (VFL). The locations of these elements are indicated by the star symbol in Fig. 3-1. These two AO devices used image metrics to correct the low-order aberrations in a custom-built program (developed by one of my colleagues Ms. Destiny Hsu). The MAL (a prototype) was designed and provided by Dr. Stefano Bonora, which can correct two astigmatisms and defocus [30]. The VFL was operated in all scaling

modes to optimize the focus on the retina while the MAL was only activated with medium and high NA modes for aberration corrections.

Meanwhile, as a part of detection, PDD (bottom left of Fig. 3-1) was employed in this system, generating DOPU contrast. Briefly, to computationally generate and analyze the depolarization effect, two orthogonally polarized inputs are required. A linear polarizer (LP), inside of the PDD, served to generate these two orthogonally polarized beams, equally dividing the input beam from the reference. Then, at the non-polarization-sensitive beam splitter, these two beams optically interfered with signals from the sample. Since this system employed a swept source, the detection channel used two balanced photodetectors were used. Therefore, it is required to divide the two interfered signals once more to sperate the two polarizations, and two polarization beam splitters (PBS) conducted this task. After passing through these two PBS, the four signals were delivered into each detector. These four input signals then were used to generate DOPU contrast.

3.2. Multi-scale and -contrast generation

As discussed in Chapter 2.2.3, multi-contrast was generated in post-processing that used DOPU signals and spatial averaging to obtain additional information. This subchapter explains how the multi-contrast map was generated from three individual input signals (OCT, OCTA, and DOPU).

Figure 3-2 illustrates the overall post-processing of generating cross-sectional OCTA (left column), regular OCT data (center column), and the combination of DOPU contrast with OCT B-scans (right column) [25]. For polarization-insensitive OCT signal generation, summation of OCT signal powers of the two channels was performed followed by averaging the multiple volumes (BM-scans) to increase the dynamic range [8], [53]. The noise-corrected DOPU rainbow map was achieved by applying the noise-error estimation that cancels the residual noise and obtains true Stokes parameters [29], [54]. This DOPU map was then multiplied with a log-scaled OCT, which was previously averaged from multiple B-scans. In the case of OCTA generation, the coherent composition process refers a phase-corrected OCT data by the use of a phase-calibration unit. The phase error correction allows a coherent temporal averaging to enhance the OCTA quality, and complex variance of OCT signals was used to calculate the motion contrast in the vascular region [53].

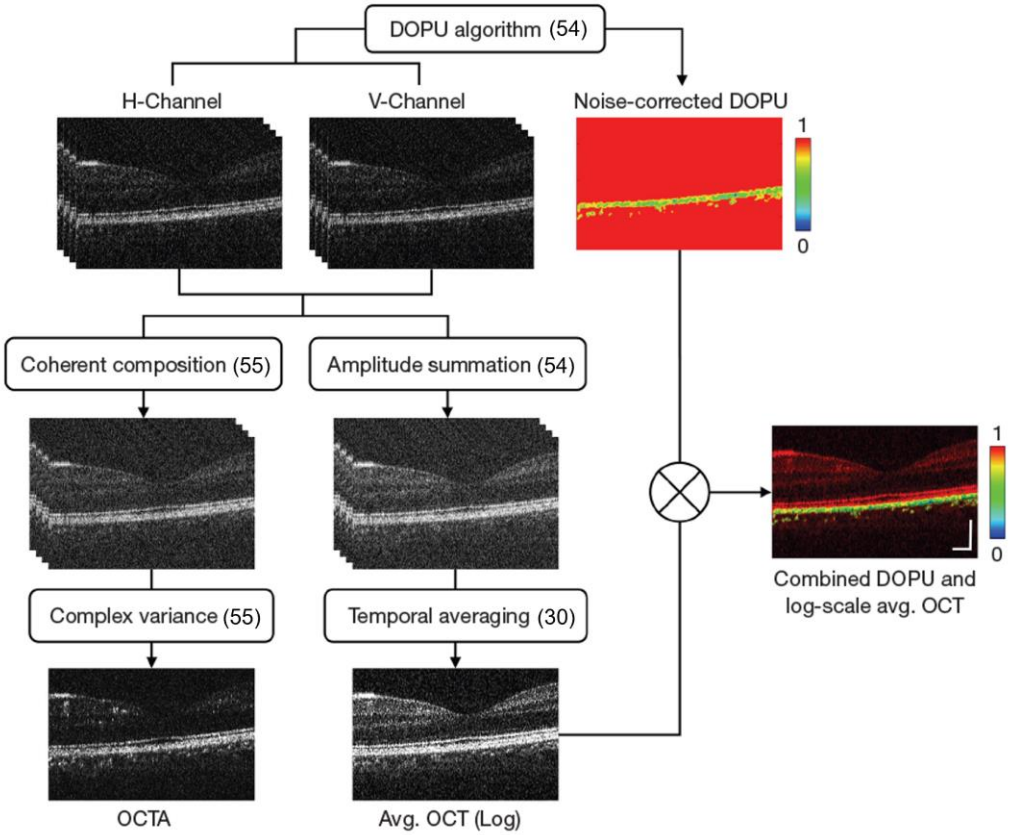

Figure 3-2 Illustrative flow chart of multi-contrast *en face* generation.

Figure 3-3 illustrates the *en face* map generation for medium and small FOV imaging modes with corresponding NA. The automated segmentation was implemented for the OCTA lateral scan, mapping the depth between the inner limiting membrane (ILM) and outer plexiform layers (OPL) [53]. The imaging protocol that was applied in this FOV mode was 4BM-scans (4 consecutive B-scans M-mode) which contains 500 A-lines and 500 B-scans (averaging 4 times), taking around 10s for each acquisition with a 100kHz swept laser source. For the large FOV mode (9 × 9 mm), OCTA contrast was not applied due to the longer scanning time that is required for imaging the large. Based on the Nyquist theorem, the adequate sampling point of this FOV is 1000 A-lines and 1000 B-scans. Thus, the scanning duration is too long to acquire a good vascular image, if BM-mode is applied. Though it was not possible to visualize the vascular information in this mode, the transversal resolution (~18 μm) was sufficient to provide large vasculatures as well as structural information based on [55].

For the generation of the *en face* projection of the RPE layer, a certain point that exhibits a low DOPU value was located by using a threshold value (0.95). This threshold value was empirically depicted in our experiments. The white arrow in the DOPU-B-scans of the bottom row indicates a relative depth profile of these points in each A-line (axial direction). These depth profiles in each lateral location were then visualized in color-coded (red to blue) on the *en face* image as it is shown in Fig. 3-3. On the *en face* image, the blue color corresponds to a relatively deeper location, compared to the other regions with yellow or reddish colors. Finally, the multi-contrast image was generated by overlaying the two *en face* images (OCTA and RPE elevation), providing both vasculature and structure information within a single image. If the pathological case has detachment or dysfunction of the RPE layer, the elevation map reveals this region with different colors.

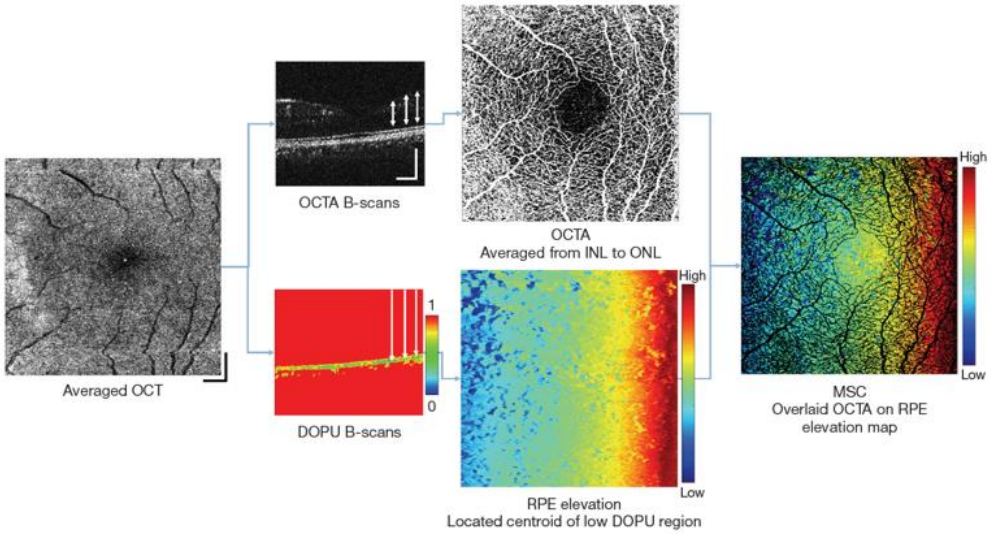

Figure 3-3 Illustrative flow chart of multi-contrast *en face* generation.

3.3. Representative Data

Figure 3-4 shows representative images from a pathological subject, displaying fundus OCT *en face* projection (A) and multi-contrast image ranging from wide (B) to narrow FOV (D). As described in the previous section, the yellow or reddish color is revealed at the center location in each FOV, indicated by white arrows. It is supposed that these colors (yellow bumps) are revealed due to the abnormal shape of the RPE layer. Similar two small 'bumps' (possibly drusen) were also exhibited in the corresponding cross-sectional image. Additionally, high-resolution blood vessel

information can be found in each FOV, due to the multi-scale mode. In the multi-contrast image of wide FOV (B), the vessel color is white (dark in other FOVs) because the OCTA imaging module was not applied in this FOV. On the top left of each multi-contrast *en face* image, a form of a wavefront is visualized. This indicates the induced waveform to correct the aberration in each imaging mode. As discussed in the system overview, VFL was applied in wide (B), and medium (C) FOV to correct defocus. The MAL was additionally applied in narrow (D) FOV to correct two astigmatisms and optimize the defocus.

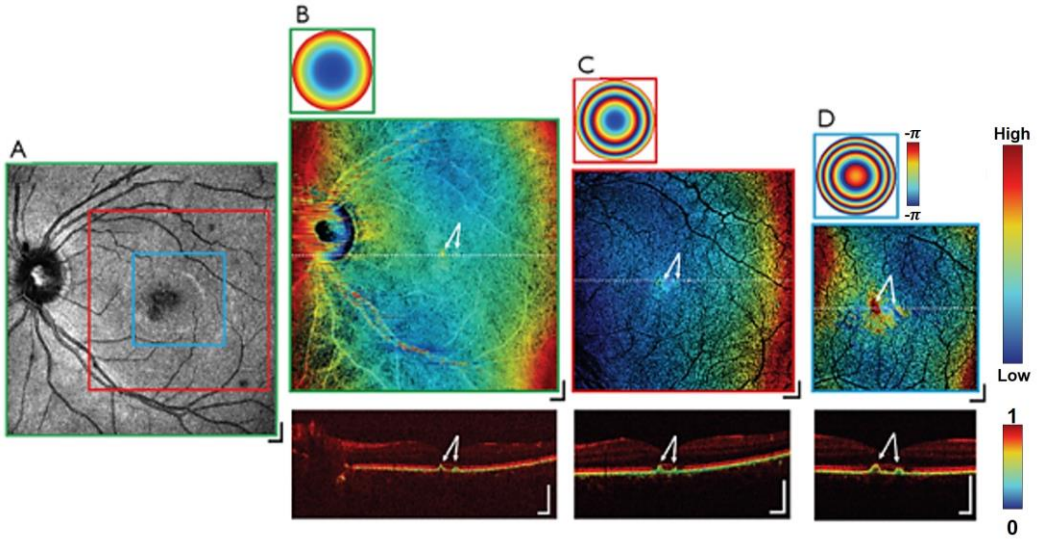

Figure 3-4 Multi-contrast *en face* data of pathological case.

Even though this OCT device successfully provided various information in a single image, the imaging FOV was limited up to 9 × 9 mm which is still small compared to the clinical demand for ultrawide field imaging. Furthermore, the relatively slow speed of the sweeping laser (100kHz) also required a longer acquisition time of approximately 12 seconds in each volume. This is not reasonable in the clinic, as there would be too much motion artifact. Therefore, this pilot study leads to develop an advanced version of the device that can enable wider FOV imaging mode and higher resolution with aberration correction.

3.4. Chapter Summary

In this chapter, a pilot study is described that demonstrated multi-scale features for retinal imaging with AO and successfully generated multi-contrast *en face* images to enhance the resolution and provide valuable information for clinicians. The project was a proof of concept for this thesis and provided the blueprint of the current system design for wider FOVs. The following chapter is for the experiments and results to understand and characterize the FDML laser source, and to seek the optimum optical system design, and possible scanning protocols.

Chapter 4. Advanced Multi-scale and -contrast Retinal OCT

4.1. Introduction

This chapter describes the design and associated experimental results of an advanced OCT system, improved from the system discussed in the previous chapter. As discussed in Chapter 1, the main goal of this advanced multi-scale and high-speed/resolution OCT (MS-HSR-OCT) device is to achieve wider FOV and faster image acquisition while maintaining multi-scale modality.

Ultra-wide FOV OCT provides more structural information within a single picture but there are several obstacles to overcome. Among them, vignetting is a phenomenon that hinders image quality due to the mismatch of focal points between two scanning mirrors (fast and slow axis) in the interferometer [27], [28], [56]. To alleviate this issue, several research reports suggested separating the fast and slow axis scanners [26], [40], [56]. Though this approach is inconvenient in that an additional lens relay is to be inserted, it reduces the computational cost of stitching multiple volumes. A similar approach is used in our research and details will be discussed in Section 4.1.

To achieve ultrahigh-speed imaging, the FDML laser was implemented in this thesis. Section 4.2 and 4.3 includes the related experiment with FMDL for system validation. Due to the limited lab access during the pandemic, it was not practically possible to build the suggested system. Instead, we used a simple OCT system that was previously used in Ref. [53] which has similar capabilities that are presented in this project. Section 4.2 explains the results of the phase stability of the FDML laser which was discussed in Chapter 2.2.1. Section 4.3 provides associated experimental results of OCTA data which is acquired by FDML laser. A brief introduction of the phase unwrapping technique that is used in Section 4.2 is discussed in the Appendix.

4.2. ZEMAX simulation of the multi-scale system

The main goal of this subchapter is to find the optimal design of an OCT engine which is advanced from our previous system in Chapter 3 by using ZEMAX simulation. The suggested design in this section provides higher resolution and wider FOV compared to our previous system. High resolution can be achieved by using a multi-scale approach that allows adjustment of the beam diameter from ~1 (low NA) to ~3 mm (high NA) and additionally, a deformable mirror (DM) for aberration correction. The design goal for wider FOV was aimed at more than 45 degrees, which is approximately twice that of the standard macular cube currently used clinically. This wide FOV can be achieved by separating the two scanning mirrors. Two representative systems (A and B) will be discussed to compare each other and several limiting factors that hinder the performance of these systems will be presented in this section.

The overview of the two system designs is shown in Fig. 4-1. System A was constructed with the two galvanometer scanners in a single XY mount. The major difference in system B is the separation of the scanner mirrors, which was implemented as shown in Fig. 4-1. (b), with an extra lens relay inserted to optically conjugate the two mirrors (X- and Y-scanner). The overall estimated size of system A in Fig. 4-1 (a) is 14.2" × 10.0" and system B in Fig. 4-1 (b) is slightly larger at 19.7" × 10.0".

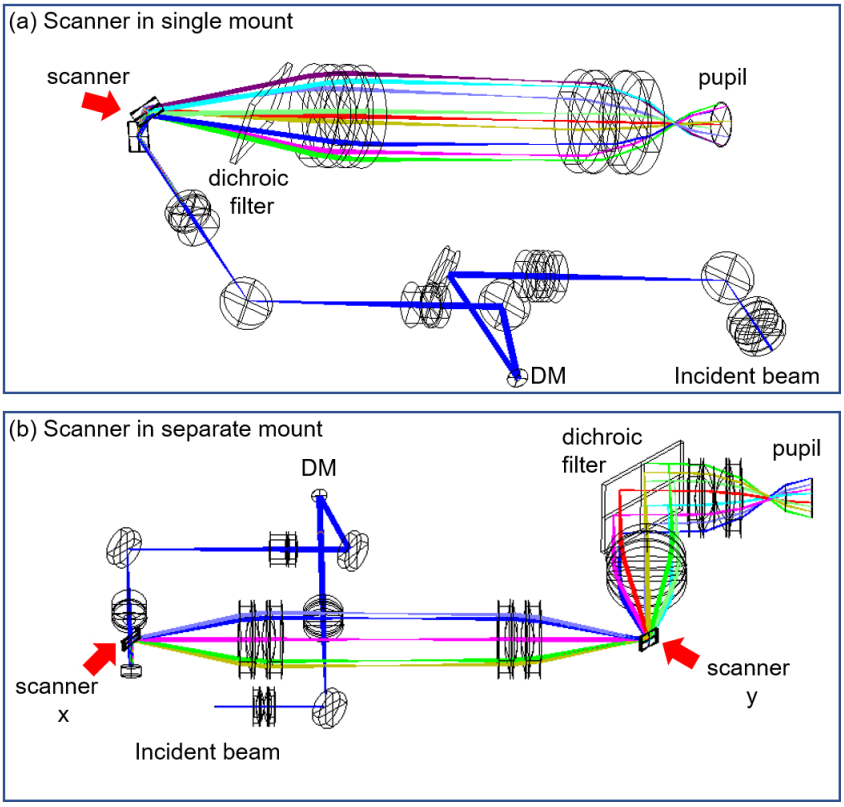

Figure 4-1 Overview of sample arm schematic of two systems; (a) two scanners in a single mount and (b) scanner is separated. Scanner locations are indicated with red arrows.

The optical elements used in both systems are listed in Table 4-1. The beam diameter listed in the right column of Table 4-1 (a) and (b) indicates the size of the beam which was determined by the magnification ratio in each relay component for the two simulated setups. The identical AO device and scanning mirror parameters are used for both systems in this simulation. The lens relay before the DM was set with a magnification to match the diameter of the incident beam to the clear aperture of this mirror (10.5 mm). However, this increases the size of the beam in low NA mode and, hinders the diffraction-limited wide FOV condition in low NA. All lens components in this system were achromatic. For the scanning mirrors, the clear aperture of these components in both systems were set to 8 mm to enable the multi-scale and wider FOV capabilities. A larger than commonly used mirror was needed to accommodate the high NA mode in a compact footprint. However, if the size of the scanning mirror is too high, the mechanical speed of the motors is limited and unstable. After several preliminary simulations, 8 mm Galvano scanning mirrors gave the best performance in our system and the design decision was made to proceed with this specification.

The difference between the two systems is the separation of the two scanning mirrors (X and Y) and therefore system B includes an additional optical relay. In system B, these lenses serve to deliver the light from the X scanner to the Y scanner with minimal loss and aberrations. Hence, in principle, system B provides wider FOV by alleviating vignetting issues at the pupil (due to unconjugated mirror planes) compared to system A. However, this lens pair is relatively sensitive, inducing an optical error that hinders the diffraction-limited condition in high NA mode. Based on the experiments with various lens pairs, stacked 2-inch lenses (75 mm focal length) provided the optimal result (in both low and high NA).

Table 4-1 Comparison of the beam profiles of the two simulated systems.

(a) System A (single mount)

Focal length (mm)	Beam diameter ($1/e^2$) (high NA / low NA) (mm)
Zoomable collimator	(3.9 / 1.27)
f_1 = 37.5	(10.5 / 3.38)
f_2 = 100	
Deformable mirror	
f_3 = 100	(7.88 / 2.54)
f_4 = 75	
Scanner	
f_5 = 100	(2.96 / 0.96)
f_6 = 37.5	

(b) System B (separated mount)

Focal length (mm)	Beam diameter ($1/e^2$) (high NA / low NA) (mm)
Zoomable collimator	(3.9 / 1.27)
f_1 = 37.5	(10.5 / 3.38)
f_2 = 100	
Deformable mirror	
f_3 = 100	(7.88 / 2.54)
f_4 = 75	
Scanner X	
f_5 = 75	(7.88 / 2.54)
f_6 = 75	
Scanner Y	
f_7 = 100	(2.96 / 0.96)
f_8 = 37.5	

Figure 4-2 illustrates the system performance comparison of two systems (A and B) in each FOV including the associated resolutions. Figure 4-2 (a) shows the possible maximum diffraction limited angle with each NA mode that is listed in the right top corner for both systems. For the high NA modes, the diffraction-limited angle of on/off axes in each system is similar to each other as the diameters of the incident beams were identical (2.96 mm in Table 4-1). Similar results have been shown with low NA modes. Figure 4-2 (b) shows the spot diagrams taken at the pupil (5 mm) of the low NA mode and each input beam in the diagram was controlled by adjusting the angle of two scanning mirrors. The second row shows the maximum angle without vignetting issue

and system B (right) gives a better angle compared to system A (left). These results show the separation of the two scanning mirrors alleviated the vignetting issue (~ 5 degrees). Comparing the two systems (A and B) designed in this thesis, system B has better performance, providing a wider scannable angle. Therefore, compared to our previous system in Chapter 3, the achievable angle is increased by ~ 12 degrees based on system B.

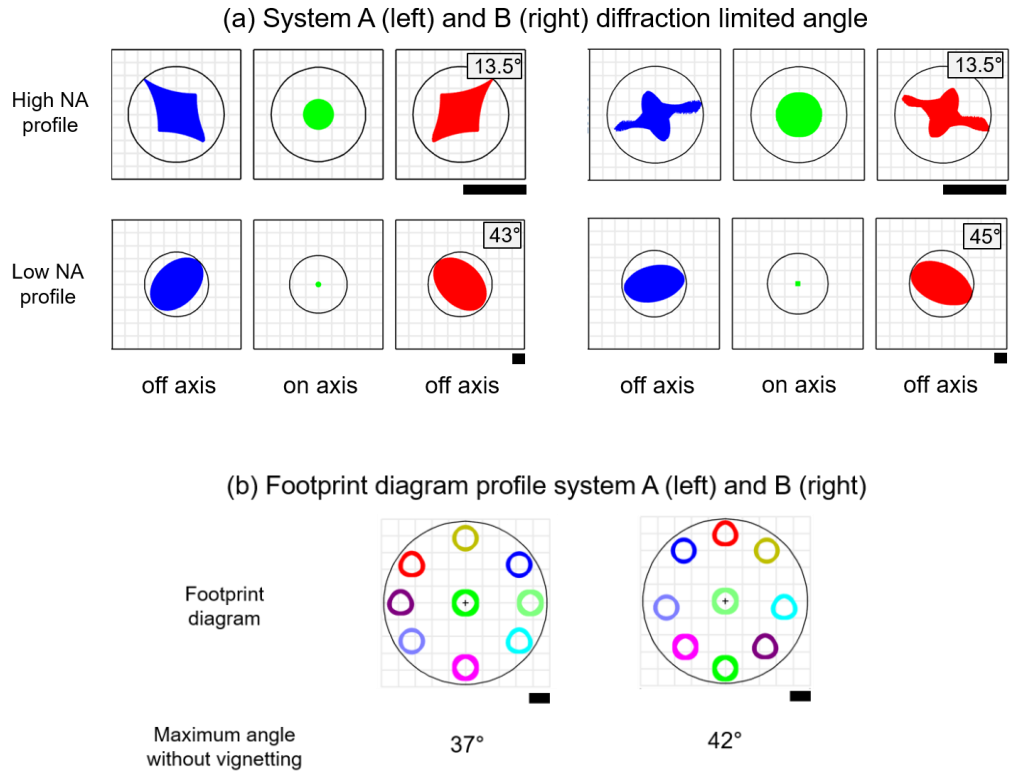

Figure 4-2 Simulated diffraction limited angle of both systems with ZEMAX (a) (scale bar indicates 10 μm) and footprint profile with maximum angle on image plane with pupil wander (b) (scale bar indicates 1 mm). Airy diameter of system A left 14.84 μm (high NA), 48.82 μm (low NA), and system B (right) 14.54 μm (high NA), 48.25 μm (low NA). Footprint diagram was performed based on the low NA mode of both system A and B.

However, the benefit of separating the two scanning mirrors in system B is relatively low compared to other studies [56]. This is because of the optical imperfection of the lens pair between the two scanners. The system designed by Wei *et al*. [56] was compared with the suggested system B in this project. It is because the diameter of the beam of Ref. [56] was similar to system B (~ 1mm) so the direct performance comparison is feasible. Moreover, in Ref. [56], the maximum FOV was 75 degrees which

is higher than system B. Fig. 4-3 shows the schematic of the experimental design that is simulated to investigate the defocusing issue caused by relay lenses between two scanners (X and Y). The lens components of this simulation were replicated from the original design introduced in Ref. [57], a same designed that is employed in research of Wei *et al.* [56].

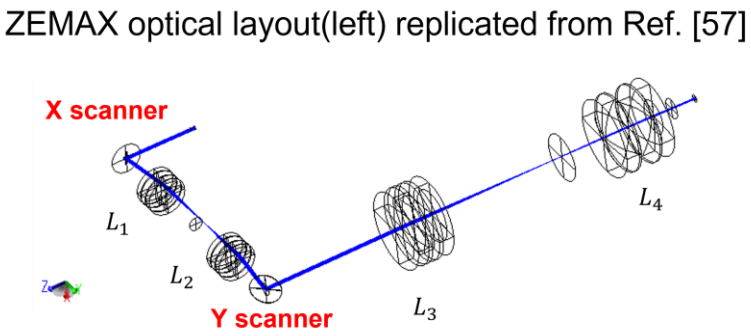

Figure 4-3 ZEMAX optical layout and corresponding footprint diagram at the pupil. Lenses $\{L_1, L_2, L_3, L_4\}$ = {37.5 mm, 37.5 mm, 100 mm, 40 mm}. The scale bar indicates 1 mm.

Figure 4-4 shows the footprint diagram of the system in Ref. [56] (left) in comparison to system B (right) as described in Fig. 4-1. The top row shows the beam profiles at scanner Y(Fig. 4-3), and settings A to D indicate the different tilt options that is applied to the scanner X. The angle that is illustrated in each Set is the value after multiplication by a factor of 2 (optical to mechanical angle). It is clearly shown that the system used by Wei *et al*. [56] has a lower displacement of the beam by tilt (see Set A) at the Y scanner. The second row displays the footprint diagram at the pupil after passing the last relay lens pair. The maximum angle of system B is similar to the system of Ref. [56] due to the difference in the demagnification ratio. System B has ~2.67 of demagnifying factor while the reference system has 2.5. This is a good result in terms of the increased demagnification ratio of the final relay lens compromised the loss of scannable area at the pupil in system B. However, due to the larger displacement of the beam at scanner Y in system B, the final FOV performance of system B is lower than the system used in Ref. [56].

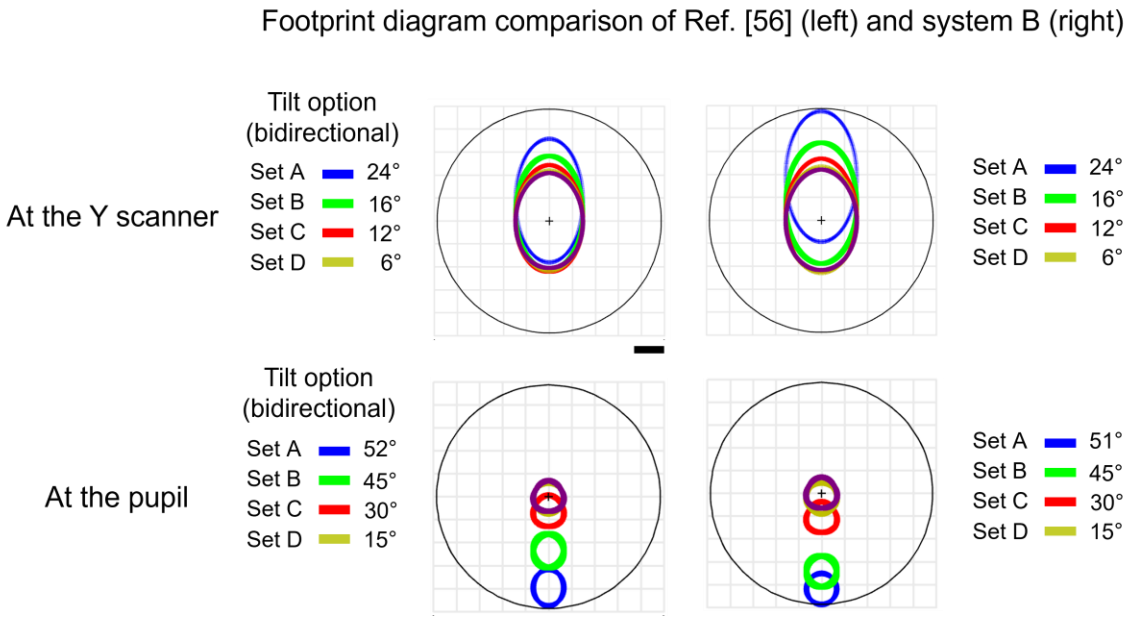

Figure 4-4 Footprint diagram comparison of the two systems (system B and Ref [56]. The footprint diagram at the scanner (top) and at the pupil (bottom) of the two systems. The scale bar indicates 1 mm (7mm pupil).

Table 4-2 shows the comparison of the lens components that are used in system B and the system proposed by Wei *et al*. [56]. The defocusing issue at the Y scanner in Fig. 4-4 of system B was relatively higher due to the larger diameter lens pair (~ 2 times) between the scanners. However, it was not possible to decrease the size of these lenses due to the need for diffraction-limited condition in the high NA mode of system B. To improve the capability of system B, more diverse lens pairs could be considered between the two scanners.

Table 4-2 Comparison of the lens materials used in system B and the system proposed by Wei *et al*. [56].

Characters	System B	System by Wei *et al*. [56]
Lens materials between the scanners	2 inch $f_1 = 75\ mm$ (150 mm × 2)	1 inch $f_1 = 37.5\ mm$ (75 mm × 2)
	2 inch $f_2 = 75\ mm$ (150 mm × 2)	1 inch $f_2 = 37.5\ mm$ (75 mm × 2)
Lens materials after the scanners	2 inch $f_1 = 100\ mm$ (200 mm × 2)	2 inch $f_1 = 100\ mm$ (200 mm × 2)
	2 inch $f_2 = 37.5\ mm$ (75 mm × 2)	2 inch $f_2 = 40\ mm$ (80 mm × 2)

Table 4-3 shows the overall performance of system B and the system of Wei *et al*. [56]. The top row shows the result of the maximum angle when only Y scanner is activated for scanning. In this case, the last relay lens of system B has a shorter focal length (37.5 mm), and this limits the maximum angle relative to the system of Ref. [56]. As discussed in the performance comparison section, there is a discrepancy in the maximum achievable FOV with each scanner. The beam delivered from the X scanner has a more defocusing issue in both systems due to the optical imperfection of the lenses between the two separated scanners This tendency was identified as higher in system B due to the larger diameter optical components. The maximum angle that system B can achieve when both mirrors (X and Y scanner) are actively scanning is lower as it is shown in the second row of Table 4-3, compared to the reference system. Similar results can be found in the research report by Wei *et al*. [56]. There is a relatively darker area (top and bottom) of the OCTA image that they provided. They suggested that this phenomenon is due to the higher sensitivity of vignetting artifacts in the vascular image. Similarly, the performance of system B in this project might be affected by the vignetting artifacts.

Table 4-3 System performance comparison of the suggested systems (A and B) and the system described by Wei *et al*. [56].

Characters	System B	System of Wet *et al*. [56]
Maximum angle with Y scanner (at the retina)	69 degrees	75 degrees
Maximum scannable angle with XY scanners (at the retina)	42 degrees	~49 degrees

4.3. Ultrahigh-speed OCT engine

Due to the lack of supply chain and limited lab access during the pandemic, unfortunately, it was not possible to build the optical system designed above and perform the validation experiments. Instead, a simple system was employed to conduct several experiments which could be useful to understand the characteristics of FDML laser. This system has been previously used in Ref. [53], and this system was slightly modified to match the specification of the current project. Figure 4-5 (a) shows the overall schematic of the system and Fig. 4-5 (b) is a topological photo. This system employed a 1.8 mm collimator, a VFL, a 3 mm galvanometer scanner pair, and one set of relay lenses. With this setup, in this subchapter, a phase stability analysis of the FDML laser, balanced photodetector comparison for dynamic range, and OCTA time interval analysis will be discussed.

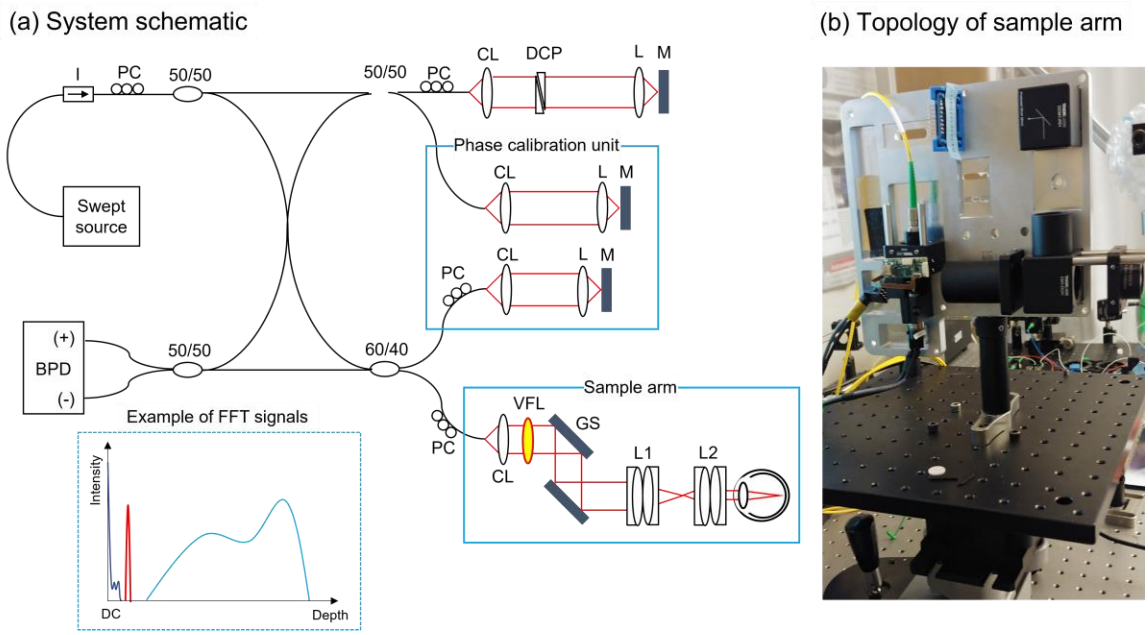

Figure 4-5 System schematic (a) and topology (b). The system delivers light into the isolator (I) to protect the laser from back reflection and four fiber couplers are employed to deliver light to each interferometer and detector. The sample arm contains VFL and two lenses $\{L_1, L_2\}$ = {50mm, 40mm}.

4.3.1. FDML Phase stability

Phase stability of the swept laser is important, and a brief introduction to understand the way to resolve this issue is discussed in the Appendix. Here, the experimental setup and its result will be described. In Fig. 4-5 (a), the phase calibration unit was used to acquire the sample mirror data for analyzing the phase stability of the FDML laser source. It was originally used in our lab to observe and correct possible jittering issues of the swept laser that operates at 100 kHz, and details of the explanation can be found in the appendix of Ref. [58]. The interference signal of the mirrors in the phase calibration unit was positioned near the DC, avoiding overlap with both the sample and the DC signal, as shown in the example of the FFT signals at the bottom of Fig. 4-5 (a).

A silver mirror was placed at the focus of the sample arm, and data were collected to extract the phase information of the source spectrum in each buffer (A-line). The phase that is measured from the phase calibration unit will be used as a baseline to correct the phase error in each buffered A-line of the main imaging interferometer. Each B-scan contains 1000 A-lines, and a total of 40 B-scans were acquired for this analysis. As is explained about the FDML laser in Appendix, applying individual rescaling vectors (polynomial function) to each buffer (B, C, D) is essential to correct residual phase shift.

Figure 4-6 (a) shows the representative unwrapped phase slopes of all buffers in wavenumber optimized by a single rescaling vector (left) and four rescaling vectors (right), respectively. Before phase unwrapping and rescaling in wavenumber, each representative A-line of each buffer was averaged by 40 B-scans to mitigate the background noise. This result indicates the multiple rescaling vectors are beneficial to minimize the phase errors but that residual phase errors still exist. Figure 4-6 (b) shows the histogram plot of estimated phase errors in each buffer by subtracting it from buffer A (reference). Each of the mean and standard deviation (std) values is indicated on the top right. Here, the phase errors from the polynomial rescaling vectors (orange) are lower than that of the phase correction with a single rescaling vector (blue). As Fig. 4-6 (b) suggests, applying 4 individual rescaling vectors was more stable and linear in k-space compared to using just a single rescaling vector for all of the buffers. Though there are still residual phase errors even after employing multiple rescaling vectors to each buffer, these residual errors could be further minimized by employing an optimization/correction function [59].

(a) Unwrapped phase slope by single vector (left) and multiple vectors (right)

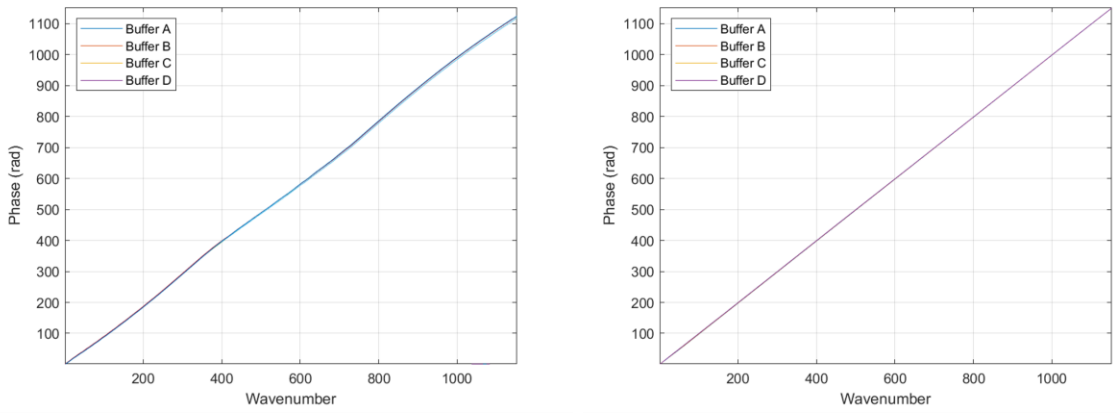

(b) Histogram of phase differences of buffer B to D subtracted from A

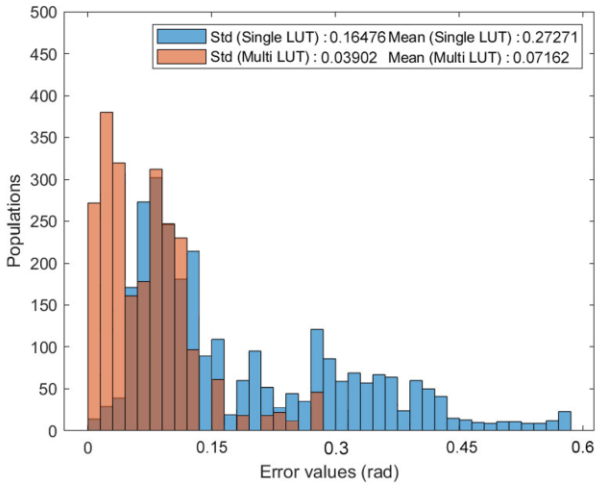

Figure 4-6 Representative unwrapped phase slopes of each buffer in wavenumber (a) and Histogram of estimated phase errors (b) comparison between single (blue) and multiple rescaling vectors (orange).

4.3.2. FDML Photodetector Selection

The performance of two balanced photodetectors (PDB481C-AC and PDB482C-AC) from Thorlabs Inc. was investigated. Table 4-4 lists the detailed information on these two photodetectors, provided on the manufacturer's website. Two experiments were performed to interpret which detector would be recommended to use in the optical

system described in this thesis. For convenience, PDB481C-AC and PDB482C-AC will be referred to as detectors (A and B), respectively.

Table 4-4 Balanced photodetector performance comparison.

Balanced photodetector information		
Characteristics	**PDB481C-AC**	**PDB482C-AC**
Internal coupling filter	HI-1060 (1060 nm fiber)	
Operating wavelength	Optimized for 1060 nm	
Coupling loss	< 1.0 dB (<0.4 dB Typically)	
Bandwidth (3dB)	30kHz ~ 1GHz	1MHz ~ 2.5 GHz
Transimpedance gain	16 × 10^3 V/A	28 × 10^3 V/A

Before the experiment, the FDML laser source spectra analysis was performed to evaluate if there are any differences between these two detectors. Figure 4-7 shows the results of the representative spectra acquired with these two devices at the same delay point. Qualitatively, Buffer A had the lowest intensity, and Buffer D had the highest; Buffers B and C look nearly identical to each other in amplitude. Here, the general shape of the signal from the two detectors are similar.

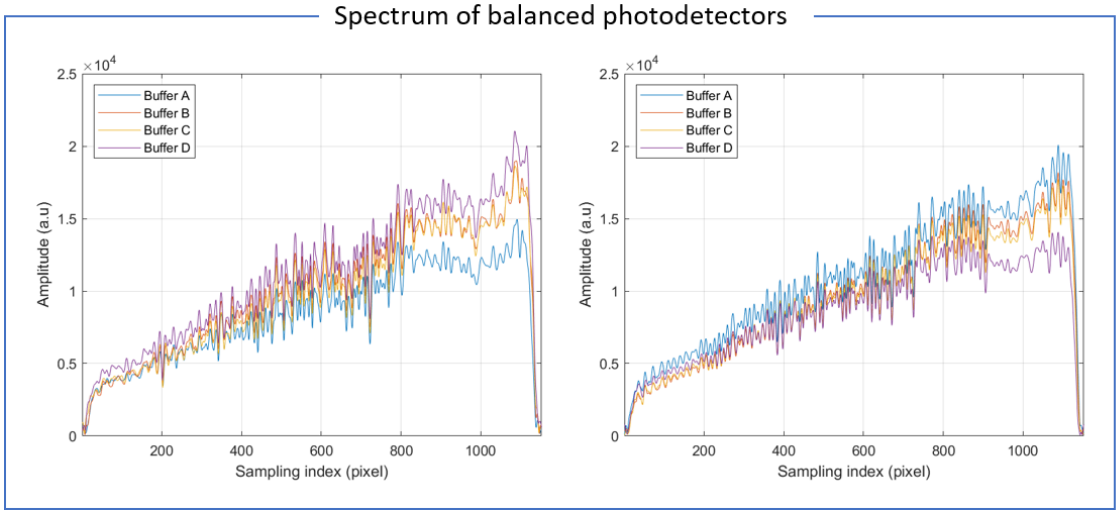

Figure 4-7 Mean plot of four buffers (A, B, C and D) of two detectors. Detector B (left) and detector A (right).

The first experiment was performed to compare the sensitivity of the two detectors. Figure 4-8 shows two OCT intensity plots of each detector along with the depth index; the signal powers were normalized with respect to detector B. The signal was collected by using the phase calibration unit which was shown in Chapter 3.1 and only the detector was replaced with one another to acquire each data. Since the gain of the detector B is higher than that of detector A, both the noise and the intensity level of detector B are relatively increased compared with detector A. Table 4-5 shows the measured sensitivity of the peak in each A-line against the standard deviation of the background noise and the sensitivity of both detectors are similar along with depth location.

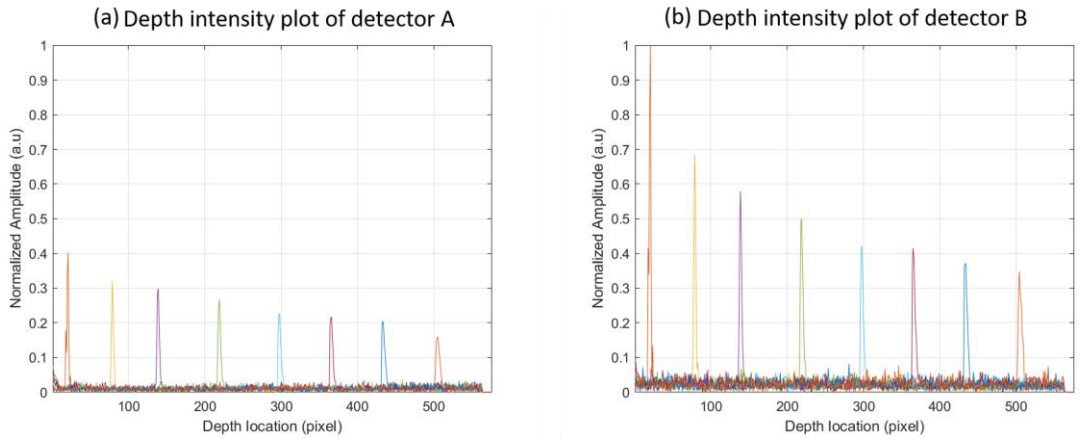

Figure 4-8 Signal plot along depth of two detectors A and B.

Table 4-5 Sensitivity comparison of two detectors A and B.

Measured sensitivity in each depth profile of detector A								
Sensitivity (dB)	21.93	19.95	19.34	18.37	16.89	16.54	16.10	13.89
Depth location (pixel)	20	79	140	221	299	365	435	504

Measured sensitivity in each depth profile of detector B								
Sensitivity (dB)	23.75	20.47	19.80	18.65	17.15	16.77	16.32	14.57
Depth location (pixel)	21	79	139	219	298	365	434	502

A second experiment was performed by a volunteer subject to compare OCT B-scans of the human retina. The incident beam power at the cornea was ~1.5mW which

is below the ANSI safety [60] and the total acquisition time was approximately 0.8 seconds that contained 800 A-lines and 1600 B-scans (2BM-scan) to average the OCT signal. The image acquisition was performed remotely via custom-made OCT software and the results of two representative OCT intensity images are displayed in Fig. 4-9. Figure 4-9 (b) shows the average intensity plots of the signal along the depth direction of the detector A (top) and B (bottom).

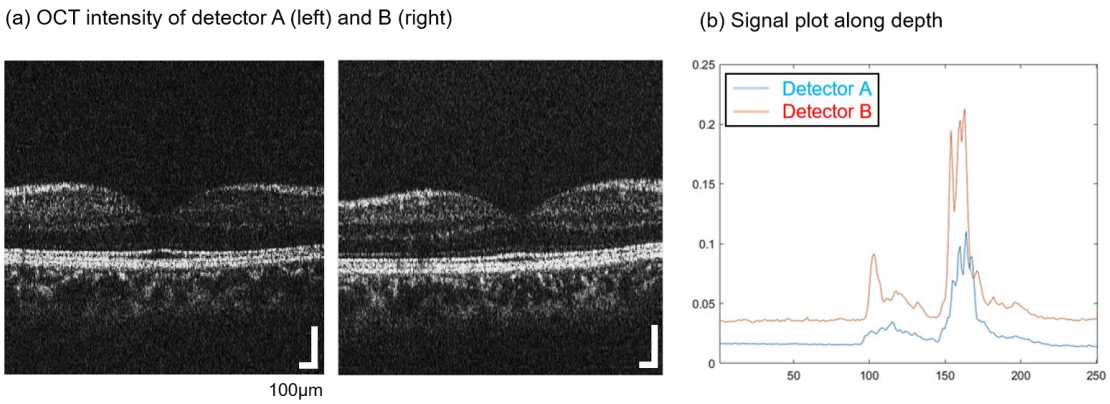

Figure 4-9 OCT intensity and mean of the signal amplitude of two detectors (A and B).

This result implies that wider bandwidth photo receiver (detector B in this case) would be beneficial for the FDML laser source. Detector B provided higher a signal amplitude that was better matched with the dynamic range of the analog-to-digital converter without introducing too much noise. With the previous two experiments, we suggest that a wider bandwidth photo receiver would provide better performance with the FDML laser source.

4.3.3. OCT Angiography with FDML

The last experiment performed with the FDML laser was to investigate the interscan time adjustment of OCTA. Since the FDML laser provides an ultrahigh-speed A-scan rate, it is possible to adjust the interscan time without sacrificing the total acquisition time. Table 4-6 shows the overall scanning protocol, and the same volunteer subject participated in this imaging session. With the FDML laser source and the current scanning protocol, a single B-scan takes 0.5 ms and the interval between consecutive B-scans used in a BM-scan can be defined in integer multiples of the single B-scan acquisition time as shown in Table 4-6. The maximum value of the inter-scan variable

setup was selected as 20 in BM-scans, corresponding to 10 ms, to investigate the effect of imaging the capillaries that are in the superficial and deep retinal capillary beds [61].

Table 4-6 Scanning protocol overview.

Imaging protocol overview

Imaging size	# of A-scans # of B-scans	B-scan Acquisition time	Lateral Resolution	Acquisition time
3 mm^2	800 1600 (2BM)	0.5 ms	10 µm	0.8 sec

Interscan protocol settings

Inter-scan time settings (Time of interscan)				
2 (1 ms)	4 (2 ms)	8 (4 ms)	10 (5 ms)	20 (10 ms)

Figure 4-10 shows the five representative OCTA *en face* images including superficial (top row) and deep capillaries (second row). The images consist of 5 volumes that were serially acquired and averaged in post-processing to enhance the image quality. The columns are sorted based on the different scanning intervals ranging from 2 to 20 B-scan intervals. For the images acquired with longer interscan delays, more vasculature can be visualized, but also more motion artifacts are present. From these experiments, the value of 8 or 10 B-scan (4 or 5 ms) interscan times is the most promising protocol to visualize the capillaries while minimizing motion artifacts.

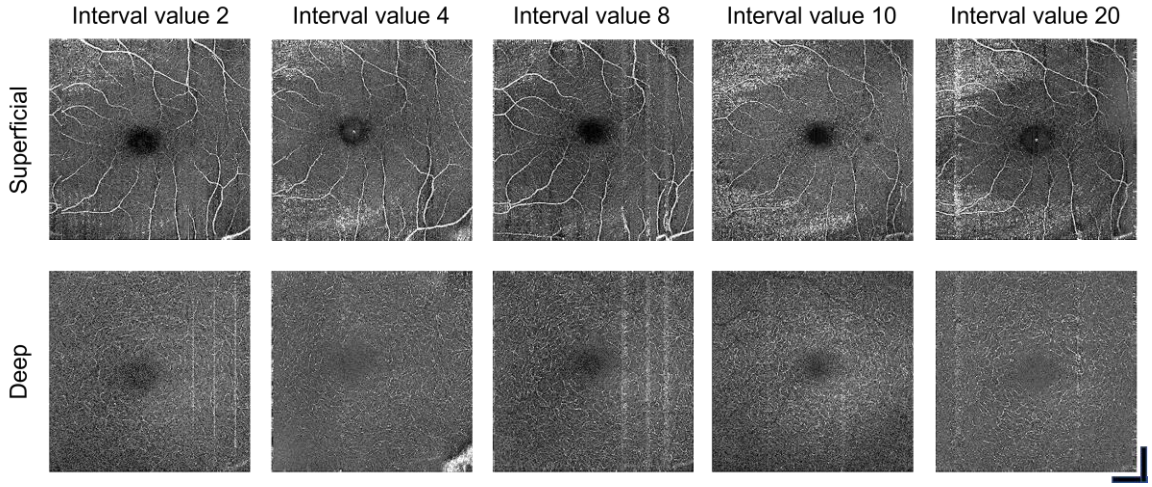

Figure 4-10 OCTA of the different interscan time modes (Inter-scan variables). Superficial layers (top row) and deep capillaries (bottom row), and scalebar is 1mm.

4.4. Chapter Summary

In this chapter, various simulations and system experiments to evaluate the performance of the multi-scale and multi-contrast imaging system. In the optical simulation, two systems with different lens configurations were compared to predict the performance. To validate the ultrahigh-speed OCT engine, a numerical phase error compensation method was applied. Finally, an OCTA analysis was performed with various interscan-time intervals to visualize the benefits of the FDML laser.

Chapter 5. Discussion and future works

This thesis was focused on simulating and understanding the development of a multi-scale and -contrast with wide field imaging system. It was unfortunate due to the COVID-19 impact, access to the lab was very limited during this time and the optical system could not be built for real experiments and demonstrations. However, still we had several beneficial experiments to validate the setup as well as investigate optical designs. In this chapter, several remaining tasks such as the imaging protocol and future considerations will be discussed.

5.1. Suggested imaging protocol

Table 5-1 shows several representative imaging modes with different FOVs and corresponding acquisition protocols. From medium to small FOVs, it is recommended to image with 4BM-scan mode to assure that the vascular information has good contrast and overcome the sensitivity penalty of the FDML laser. The number of A-scans was affected by the maximum mechanical frequency of the galvanometer mounted mirror scanners (8 mm clear aperture).

Table 5-1 Suggested imaging protocols.

Imaging mode (mm)	# of A-scans	Pupil diameter ($1/e^2$)	Lateral Resolution (grid size)	Acquisition time
Wide (12.5 × 12.5)	2000	1 mm	20 μm (8.75 μm)	2.5 sec (4sec / 2BM)
Medium (6 × 6)	1400	2 mm	10 μm (4.3 μm)	1.3 sec (5.9sec / 4BM)
Narrow (3 × 3)	1400	3 mm	~6.7 μm (2.1 μm)	1.3 sec (5.9sec / 4BM)

To achieve high NA in narrow FOVs, the size of the mirrors in each of the two scan axes must be large enough to accommodate the beam size. On the contrary, Fig. 5-1 illustrates that the larger size of the mirror has limited maximum speed that the

mirror can move (provided by the manufacturer). This limitation shows a careful selection of mirrors is required to fulfill the high-resolution imaging system.

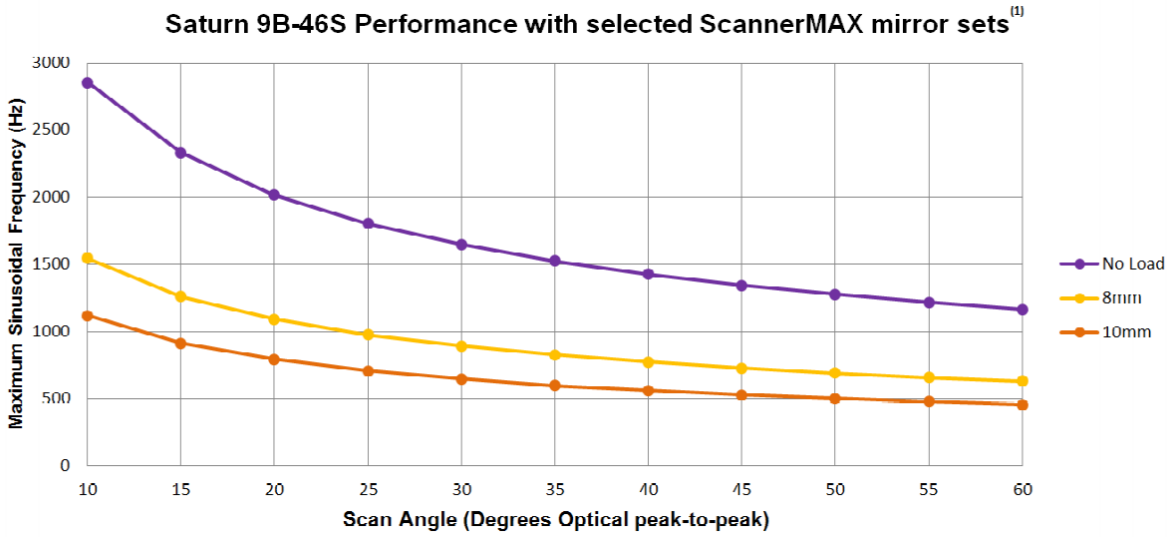

Figure 5-1 Data plot of the galvanometer scanners for maximum frequency with angles (Optical)_Reference required (image was provided from the manufacturer).

Compared to our previous system that was introduced in Chapter 3, the suggested system B in this project (Chapter 4) can achieve both multi-scale and wider FOV (~12.5 mm). Though it was not possible to develop a system that can cover over 45 degrees (13.5 mm) with off the shelf components meeting all of the requirements, this OCT engine has unique feature that can visualize high-contrast vascular information by adjusting the beam diameter. Furthermore, by utilizing the FDML laser, the image acquisition time is substantially decreased. However, we believe further exploration of diverse lens pairs (possibly customized lenses) would increase the capability of this system. One imaging modality that was not able to be employed in this project was multi-contrast and details will be discussed in the following subchapter.

5.2. Polarization diversity detection

To investigate the feasibility of multi-contrast modality with the FDML laser, the polarization diversity detection unit (PDD) used in our previous system in Chapter 3, was tested in this project. However, it was not possible in this project due to several obstacles.

First, the previously customized program was not properly synchronized with the FDML laser. The possible reason is the different mechanical behaviors (buffering stages) of the FDML laser compared to the swept laser. One of the major problems in this test was the limited time of lab access during the pandemic. The program design team participated to investigate the issue during this period but troubleshooting required more research.

Secondly, the possible signal loss by PDD is required to be investigated. In our previous study, the signal loss from the PDD was ~ 3 dB. Furthermore, since the FDML laser has a sensitivity penalty as discussed in Chapter 2.2.1, the relationships between DOPU measurement and sensitivity loss need more attention while performing multi-contrast imaging modality.

If these obstacles can be overcome, the potential of multi-scale/-contrast with the ultrahigh-speed FDML laser is promising.

5.3. Conclusion

In this thesis, the design, experimental validation, and recommended imaging protocols for a multi-scale and -contrast imaging system were presented. The experimental results demonstrated the potential of the ultrahigh-speed swept laser for a wider range of multi-scale FOVs which were not feasible with the previous system. After the system is built and ready to use, the FDML bases system has the potential to provide more benefits and understanding in retinal imaging with OCTA.

References

[1] “Michael H. Ross, Wojciech Pawlina - Histology_ A Text and Atlas_ With Correlated Cell and Molecular Biology, 6th Edition -Lippincott Williams & Wilkins (2010)”.

[2] Jessica Lee and Richard B. Rosen, “ Learning to read retinal OCT,” *Ophthalmology Management*, vol. 19, no. July 2015, pp. 44–46, Jul. 2015.

[3] S. Grover, R. K. Murthy, V. S. Brar, and K. v. Chalam, “Comparison of retinal thickness in normal eyes using stratus and spectralis optical coherence tomography,” *Invest Ophthalmol Vis Sci*, vol. 51, no. 5, pp. 2644–2647, 2010, doi: 10.1167/iovs.09-4774.

[4] S. L. S. Ding, S. Kumar, and P. L. Mok, “Cellular reparative mechanisms of mesenchymal stem cells for retinal diseases,” *International Journal of Molecular Sciences*, vol. 18, no. 8. MDPI AG, Aug. 01, 2017. doi: 10.3390/ijms18081406.

[5] N. Jain *et al.*, “Quantitative comparison of drusen segmented on SD-OCT versus drusen delineated on color fundus photographs,” *Investigative Ophthalmology and Visual Science*, vol. 51, no. 10. pp. 4875–4883, Oct. 2010. doi: 10.1167/iovs.09-4962.

[6] T. Duncker *et al.*, “Quantitative fundus autofluorescence and optical coherence tomography in ABCA4 carriers,” *Invest Ophthalmol Vis Sci*, vol. 56, no. 12, pp. 7274–7285, 2015, doi: 10.1167/iovs.15-17371.

[7] B. R. Hurley and C. D. Regillo, “2 Fluorescein Angiography: General Principles and Interpretation.”

[8] D. J. Wahl, Y. Jian, S. Bonora, R. J. Zawadzki, M. v. Sarunic, and M. v. Sarunic1, “Wavefront sensorless adaptive optics fluorescence biomicroscope for in vivo retinal imaging in mice,” *Opt Express*, vol. 7, no. 1, p. 1, 2015, doi: 10.1364/BOE.7.00001.

[9] J. Gong, S. Yu, Y. Gong, F. Wang, and X. Sun, “The diagnostic accuracy of optical coherence tomography angiography for neovascular age-related macular

degeneration: A comparison with fundus fluorescein angiography," *J Ophthalmol*, vol. 2016, 2016, doi: 10.1155/2016/7521478.

[10] Griffin Jardine, "FUNDUS PHOTOGRAPHY, FLUORESCEIN ANGIOGRAPHY, AND INDOCYANINE GREEN ANGIOGRAPHY OF TUBERCULOUS CHOROIDITIS," Utah, Nov. 2017.

[11] M. F. Kraus *et al.*, "Motion correction in OCT volumes on a per A-scan basis using orthogonal scan patterns," Springer, 2012. doi: 10.1364/BOE.3.001182.

[12] M. Pircher and R. J. Zawadzki, "Review of adaptive optics OCT (AO-OCT): principles and applications for retinal imaging [Invited]," *Biomed Opt Express*, vol. 8, no. 5, pp. 2536–2562, 2017, doi: 10.1364/BOE.8.002536.

[13] B. Imaging, *Aberrations and the Benefit of Their Correction in Confocal Microscopy*. 2013. doi: 10.1201/b14898-11.

[14] J. Lammer *et al.*, "Detection and analysis of hard exudates by polarization-sensitive optical coherence tomography in patients with diabetic maculopathy," *Invest Ophthalmol Vis Sci*, vol. 55, no. 3, pp. 1564–1571, 2014, doi: 10.1167/iovs.13-13539.

[15] S. Makita, Y.-J. Hong, M. Miura, and Y. Yasuno, "Degree of polarization uniformity with high noise immunity using polarization-sensitive optical coherence tomography," *Opt Lett*, vol. 39, no. 24, p. 6783, 2014, doi: 10.1364/ol.39.006783.

[16] B. Baumann *et al.*, "Spectral degree of polarization uniformity for polarization-sensitive OCT," *J Mod Opt*, vol. 62, no. 21, pp. 1758–1763, 2015, doi: 10.1080/09500340.2014.945501.

[17] P. Roberts *et al.*, "Retinal Pigment Epithelial Features in Central Serous Chorioretinopathy Identified by Polarization-Sensitive Optical Coherence Tomography," 2016, doi: 10.1167/iovs.15-18494.

[18] C. Ahlers *et al.*, "Imaging of the retinal pigment epithelium in age-related macular degeneration using polarization-sensitive optical coherence tomography," *Invest*

Ophthalmol Vis Sci, vol. 51, no. 4, pp. 2149–2157, 2010, doi: 10.1167/iovs.09-3817.

[19] N. Lippok, M. Villiger, and B. E. Bouma, “Degree of polarization (uniformity) and depolarization index: unambiguous depolarization contrast for optical coherence tomography,” *Opt Lett*, vol. 40, no. 17, p. 3954, Sep. 2015, doi: 10.1364/ol.40.003954.

[20] M. Sugita *et al.*, “Analysis of optimum conditions of depolarization imaging by polarization-sensitive optical coherence tomography in the human retina,” *J Biomed Opt*, vol. 20, no. 1, p. 016011, 2015, doi: 10.1117/1.jbo.20.1.016011.

[21] N. Lippok, B. Braaf, M. Villiger, W. Y. Oh, B. J. Vakoc, and B. E. Bouma, “Quantitative depolarization measurements for fiber-based polarization-sensitive optical frequency domain imaging of the retinal pigment epithelium,” *J Biophotonics*, vol. 12, no. 1, pp. 1–8, 2019, doi: 10.1002/jbio.201800156.

[22] E. Götzinger *et al.*, “Retinal pigment epithelium segmentation by polarization sensitive optical coherence tomography,” *Opt Express*, vol. 16, no. 21, p. 16410, 2008, doi: 10.1364/oe.16.016410.

[23] B. Baumann *et al.*, “Polarization sensitive optical coherence tomography of melanin provides intrinsic contrast based on depolarization,” *Biomed Opt Express*, vol. 3, no. 7, p. 1670, 2012, doi: 10.1364/boe.3.001670.

[24] B. Baumann *et al.*, “Melanin pigmentation in rat eyes: In vivo imaging by polarization-sensitive optical coherence tomography and comparison to histology,” *Invest Ophthalmol Vis Sci*, vol. 56, no. 12, pp. 7462–7472, 2015, doi: 10.1167/iovs.15-17742.

[25] M. J. Ju *et al.*, “Multi-scale and -contrast sensorless adaptive optics optical coherence tomography,” vol. 9, no. 5, pp. 757–768, 2019, doi: 10.21037/qims.2019.05.17.

[26] J. Polans *et al.*, “Wide-field retinal optical coherence tomography with wavefront sensorless adaptive optics for enhanced imaging of targeted regions,” *Biomed Opt Express*, vol. 8, no. 1, p. 16, 2017, doi: 10.1364/boe.8.000016.

[27] J. P. Kolb, T. Klein, C. L. Kufner, W. Wieser, A. S. Neubauer, and R. Huber, “Ultra-widefield retinal MHz-OCT imaging with up to 100 degrees viewing angle,” *Biomed Opt Express*, vol. 6, no. 5, p. 1534, 2015, doi: 10.1364/boe.6.001534.

[28] Q. Zhang, K. A. Rezaei, S. S. Saraf, Z. Chu, F. Wang, and R. K. Wang, “Ultra-wide optical coherence tomography angiography in diabetic retinopathy,” *Quant Imaging Med Surg*, vol. 8, no. 8, pp. 743–753, 2018, doi: 10.21037/qims.2018.09.02.

[29] D. Hsu *et al.*, “Quantitative multi-contrast in vivo mouse imaging with polarization diversity optical coherence tomography and angiography,” *Biomed Opt Express*, vol. 11, no. 12, p. 6945, 2020, doi: 10.1364/boe.403209.

[30] S. Bonora *et al.*, “Wavefront correction and high-resolution in vivo OCT imaging with an objective integrated multi-actuator adaptive lens,” *Opt Express*, vol. 23, no. 17, p. 21931, 2015, doi: 10.1364/oe.23.021931.

[31] Y. Jian *et al.*, “Lens-based wavefront sensorless adaptive optics swept source OCT,” *Sci Rep*, vol. 6, no. May, pp. 1–10, 2016, doi: 10.1038/srep27620.

[32] H. R. G. W. Verstraete *et al.*, “Wavefront sensorless adaptive optics OCT with the DONE algorithm for in vivo human retinal imaging [Invited],” *Biomed Opt Express*, vol. 8, no. 4, p. 2261, 2017, doi: 10.1364/BOE.8.002261.

[33] J. G. Fujimoto, *Optical coherence tomography: Technology and applications*. 2002. doi: 10.1109/OMEMS.2002.1031485.

[34] B. Braaf, “The principles of Optical Coherence Tomography for posterior eye imaging,” *Principles of OCT*, pp. 13–34, 2015.

[35] G. Keiser, *Biophotonics: Concepts to Applications*. 2016.

[36] J. L. Sandell and T. C. Zhu, “A review of in-vivo optical properties of human tissues and its impact on PDT.”

[37] X. Wang *et al.*, “A simple system of swept source optical coherence tomography for a large imaging depth range,” *Opt Commun*, vol. 431, pp. 51–57, 2019, doi: 10.1016/j.optcom.2018.08.080.

[38] S. T. Ross, J. R. Allen, and M. W. Davidson, *Practical considerations of objective lenses for application in cell biology*, 1st ed., vol. 123. Elsevier Inc., 2014. doi: 10.1016/B978-0-12-420138-5.00002-1.

[39] V. Jayaraman *et al.*, “Recent advances in MEMS-VCSELs for high performance structural and functional SS-OCT imaging,” in *Optical Coherence Tomography and Coherence Domain Optical Methods in Biomedicine XVIII*, SPIE, Mar. 2014, p. 893402. doi: 10.1117/12.2041718.

[40] T. Klein, W. Wieser, L. Reznicek, A. Neubauer, A. Kampik, and R. Huber, “Multi-MHz retinal OCT,” *Biomed Opt Express*, vol. 4, no. 10, p. 1890, 2013, doi: 10.1364/boe.4.001890.

[41] J. v. Migacz, I. Gorczynska, M. Azimipour, R. Jonnal, R. J. Zawadzki, and J. S. Werner, “Megahertz-rate optical coherence tomography angiography improves the contrast of the choriocapillaris and choroid in human retinal imaging,” *Biomed Opt Express*, vol. 10, no. 1, p. 50, 2019, doi: 10.1364/boe.10.000050.

[42] “Title: NG-FDML-User Guide NG-FDML User Guide.”

[43] W. J. Choi *et al.*, “Choriocapillaris and choroidal microvasculature imaging with ultrahigh speed OCT angiography,” *PLoS One*, vol. 8, no. 12, 2013, doi: 10.1371/journal.pone.0081499.

[44] A. Athwal, C. Balaratnasingam, D.-Y. Yu, M. Heisler, M. v. Sarunic, and M. J. Ju, “Optimizing 3D retinal vasculature imaging in diabetic retinopathy using registration and averaging of OCT-A,” *Biomed Opt Express*, vol. 12, no. 1, p. 553, 2021, doi: 10.1364/boe.408590.

[45] M. Szkulmowski and M. Wojtkowski, “Averaging techniques for OCT imaging,” *Opt Express*, vol. 21, no. 8, p. 9757, 2013, doi: 10.1364/oe.21.009757.

[46] J. Liang and D. R. Williams, “Aberrations and retinal image quality of the normal human eye,” *Journal of the Optical Society of America A*, vol. 14, no. 11, p. 2873, 1997, doi: 10.1364/josaa.14.002873.

[47] N. Maeda, “Clinical applications of wavefront aberrometry - A review,” *Clin Exp Ophthalmol*, vol. 37, no. 1, pp. 118–129, 2009, doi: 10.1111/j.1442-9071.2009.02005.x.

[48] Y. Jian, J. Xu, M. A. Gradowski, S. Bonora, R. J. Zawadzki, and M. v. Sarunic, “Wavefront sensorless adaptive optics optical coherence tomography for in vivo retinal imaging in mice,” *Biomed Opt Express*, vol. 5, no. 2, p. 547, 2014, doi: 10.1364/boe.5.000547.

[49] D. J. Wahl *et al.*, “Two photon imaging of mouse retina with sensorless adaptive optics,” *2016 IEEE Photonics Conference, IPC 2016*, pp. 130–131, 2017, doi: 10.1109/IPCon.2016.7831010.

[50] T. E. de Carlo, A. Romano, N. K. Waheed, and J. S. Duker, “A review of optical coherence tomography angiography (OCTA),” *International Journal of Retina and Vitreous*, vol. 1, no. 1. BioMed Central Ltd., Jul. 24, 2015. doi: 10.1186/s40942-015-0005-8.

[51] M. Pircher *et al.*, “Human macula investigated in vivo with polarization-sensitive optical coherence tomography,” *Invest Ophthalmol Vis Sci*, vol. 47, no. 12, pp. 5487–5494, Dec. 2006, doi: 10.1167/iovs.05-1589.

[52] S. Makita, T. Mino, T. Yamaguchi, M. Miura, S. Azuma, and Y. Yasuno, “Clinical prototype of pigment and flow imaging optical coherence tomography for posterior eye investigation,” *Biomed. Opt. Express*, vol. 9, no. 9, pp. 1564–1571, 2018.

[53] M. J. Ju, M. Heisler, A. Athwal, M. v. Sarunic, and Y. Jian, “Effective bidirectional scanning pattern for optical coherence tomography angiography,” *Biomed Opt Express*, vol. 9, no. 5, p. 2336, 2018, doi: 10.1364/boe.9.002336.

[54] S. Makita, Y.-J. Hong, M. Miura, and Y. Yasuno, “Degree of polarization uniformity with high noise immunity using polarization-sensitive optical coherence tomography,” *Opt Lett*, vol. 39, no. 24, p. 6783, Dec. 2014, doi: 10.1364/ol.39.006783.

[55] D. Goldenberg, J. Shahar, A. Loewenstein, and M. Goldstein, “DIAMETERS OF RETINAL BLOOD VESSELS IN A HEALTHY COHORT AS MEASURED BY

SPECTRAL DOMAIN OPTICAL COHERENCE TOMOGRAPHY.” [Online]. Available: http://rsb.info.nih.gov/ij

[56] X. I. W. Ei, T. R. T. H. Ormel, and Y. U. G. Uo, “75 degree non-mydriatic signle-volume optical coherence tomography angiography,” vol. 10, no. 12, pp. 6286–6295, 2019.

[57] X. Wei, T. T. Hormel, S. Pi, Y. Guo, Y. Jian, and Y. Jia, “High dynamic range optical coherence tomography angiography (HDR-OCTA),” *Biomed Opt Express*, vol. 10, no. 7, p. 3560, 2019, doi: 10.1364/boe.10.003560.

[58] M. J. Ju *et al.*, “Advanced multi-contrast Jones matrix optical coherence tomography for Doppler and polarization sensitive imaging,” *Opt Express*, vol. 21, no. 16, p. 19412, 2013, doi: 10.1364/oe.21.019412.

[59] Y. Miao *et al.*, “Phase-corrected buffer averaging for enhanced OCT angiography using FDML laser,” *Opt Lett*, vol. 46, no. 16, p. 3833, Aug. 2021, doi: 10.1364/ol.430915.

[60] S. Rees and G. Dobre, “Maximum permissible exposure of the retina in the human eye in optical coherence tomography systems using a confocal scanning laser ophthalmoscopy platform,” *Fifth International Conference on Lasers in Medicine: Biotechnologies Integrated in Daily Medicine*, vol. 8925, p. 89250N, 2014, doi: 10.1117/12.2044819.

[61] P. Bedggood and A. Metha, “Mapping flow velocity in the human retinal capillary network with pixel intensity cross correlation,” *PLoS One*, vol. 14, no. 6, pp. 1–22, 2018, doi: 10.1371/journal.pone.0218918.

[62] B. J. Vakoc, S. H. Yun, J. F. de Boer, G. J. Tearney, and B. E. Bouma, “Phase-resolved optical frequency domain imaging,” *Opt Express*, vol. 13, no. 14, p. 5483, 2005, doi: 10.1364/opex.13.005483.

[63] W. Choi *et al.*, “Phase-sensitive swept-source optical coherence tomography imaging of the human retina with a vertical cavity surface-emitting laser light source,” *Opt Lett*, vol. 38, no. 3, p. 338, 2013, doi: 10.1364/ol.38.000338.

[64] J. Fingler, R. J. Zawadzki, J. S. Werner, D. Schwartz, and S. E. Fraser, “Volumetric microvascular imaging of human retina using optical coherence tomography with a novel motion contrast technique,” *Opt Express*, vol. 17, no. 24, p. 22190, 2009, doi: 10.1364/oe.17.022190.

[65] Y. Yasuno *et al.*, “Three-dimensional and high-speed swept-source optical coherence tomography for in vivo investigation of human anterior eye segments,” *Opt Express*, vol. 13, no. 26, p. 10652, 2005, doi: 10.1364/opex.13.010652.

Appendix A. Analysis of phase in complex OCT

Since the FDML laser sweeps an instantaneously narrowband filter over a broader wavelength range over time, a mismatch/variation in the synchronization of the FDML laser to the data acquisition device induces a phase error. This severely impacts the quality of the OCT angiogram. Several research groups studied various methods to resolve this issue [62]–[64]. Here, a simple numerical compensation method by polynomial optimization was employed in this thesis [65] and a brief introduction of phase error estimation based on the complex signal will be discussed in this section. Further hardware implementation and representative experiments to visualize the result is explained in Chapter 4.3.

First, a general explanation of the complex signal acquired in FD-OCT will be introduced. Equation 1 shows the overall mathematical terms that are measured by FD-OCT where I_D is Fourier domain signal, $\tau = z/c$ (c is the speed of light and z optical axis), $\gamma(\tau)$ denotes the normalized temporal coherence function ($\Gamma(\tau)/\Gamma(0)$), ρ_i and ρ_R are the reflectivity of the sample and reference mirror, I_0 is the power of the incident light source, δ is the Dirac delta function of τ in ith and jth index along optical axis, $\otimes$ is convolution, and $c.c.$ denotes complex conjugate [33]. The Fourier domain signal I_D contains three terms (DC, autocorrelation, and structural information) [33].

$$
\begin{aligned}
|I_D(\tau)| \propto\ & I_0|\gamma(\tau)|\left[\sum_i |\rho_i|^2 + |\rho_R|^2\right] + I_0|\gamma(\tau)| \\
& \otimes \left[\sum_{i,j;i>j} \rho_i \rho_j^* \delta\left[\tau - \left(\tau_i - \tau_j\right)\right]\right. \\
& \left. + \sum_i \rho_i \rho_R^* \delta[\tau - (\tau_i - \tau_R)]\right] + c.c.
\end{aligned}
\qquad \text{Eq. 1}
$$

The first term (DC) is generated by the non-interfering component of the sample/reference arm and in SS-OCT, this term can be neglected when using balanced photodetection. The second term (autocorrelation) can also be neglected, and details can be found in Chapter 6 in Ref. [33]. Finally, the c.c. is the complex conjugate artifact which is a signal but reflected with respect to the zero-delay. This term can be cropped

by using only the positive side of the interference signals after the Fourier transform of the fringe signals.

Figure A illustrates the schematic of post-processing to extract the phase information from the source spectrum. On the top left, the raw data of each A-line is shown. The Hilbert transform can be implemented to generate the imaginary part of the signal. Then, by applying Fourier transformation, the sample data can be easily identified by the higher intensity relative to the noise, as shown. To remove the background noise and extract the source spectrum of the sample, a simple windowing function can be applied to this data. Lastly, the inverse Fourier transform is applied into the windowed signal.

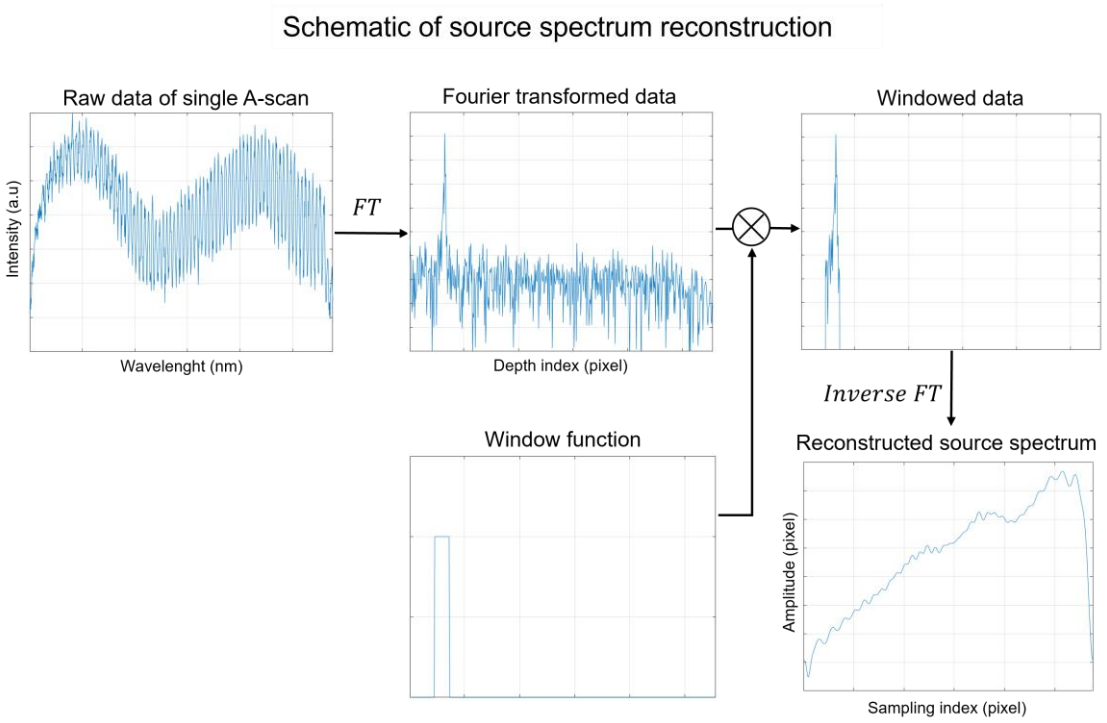

Figure A.1. Schematics of the spectrum reconstruction from complex signals.

In case of the FDML laser, Figure B (a) shows conceptual image of a single B-scan that contains multiple A-lines, including buffers. A similar way of the phase extraction from the complex signals can be applied to the FDML data. By performing the same steps from Fig. A on each buffer, Fig. B (b) illustrates the source spectra that is extracted from a series of 4 buffered A-lines. As discussed in Chapter 2.2.1 and Chapter

4.3.1, the phase of each buffer (A to D) is not identical to each other. Therefore, it is essential to generate individual timing vectors when rescaling each buffer to linearize the sampling index (time domain) to the wavenumber (k-space). This can be done by using polynomial timing delay vectors and adding an additional timing delay term to each [59]. This linearization process can provide the phase-resolved depth profiles for a FDML laser OCT engine and generate high quality OCTA images.

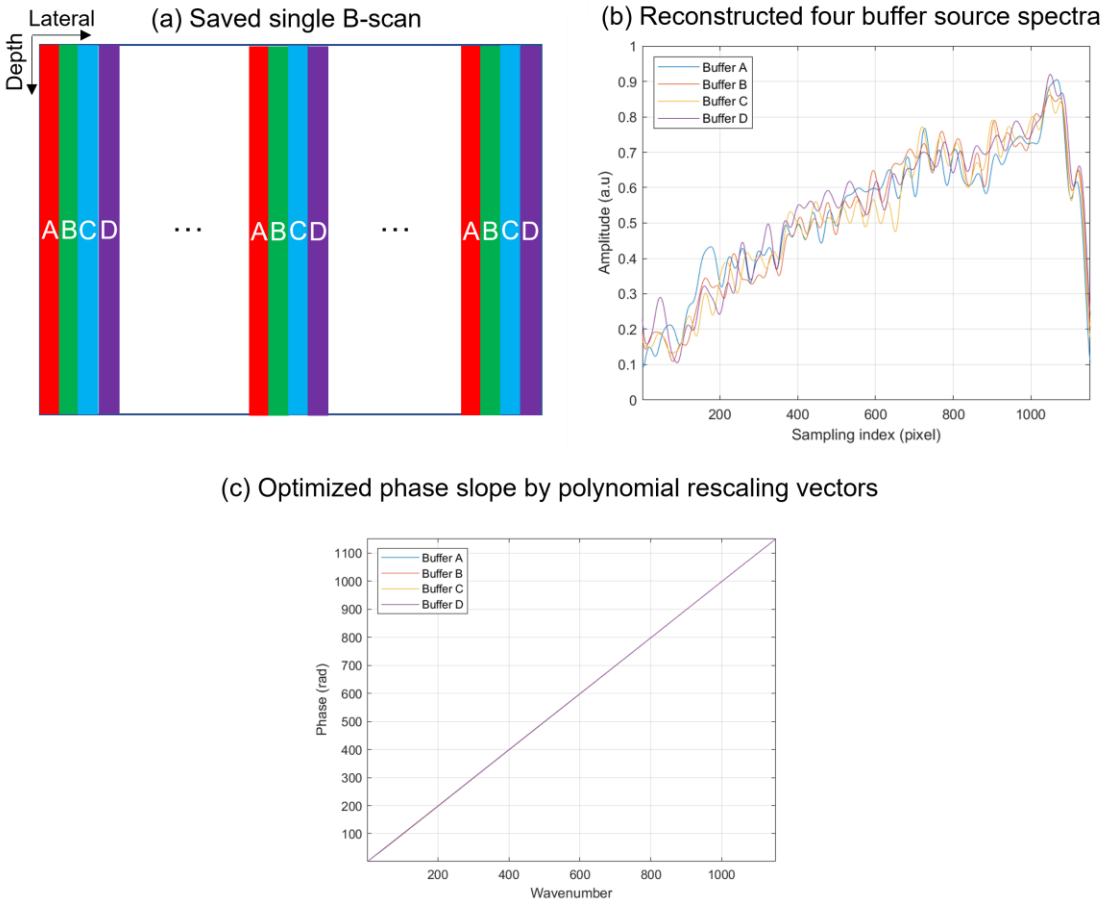

Figure A.2. The buffer profiles contained in a series of A-lines (B-scan) in OCT acquired with FDML laser (a). A generated sample buffer spectrum (b) and a representative phase slope of each buffer in wavenumber by applying rescaling vectors (d).